J. Fluid Mech. (2002), *vol.* 472, *pp.* 83–124.
DOI: 10.1017/S0022112002002094 Printed in the United Kingdom

Experiments on stability and transition at Mach 3†

By PAOLO GRAZIOSI‡ AND GARRY L. BROWN

Department of Mechanical and Aerospace Engineering, Princeton University, Princeton, NJ 08544, USA

(Received 17 July 2001 and in revised form 20 June 2002)

The results of an experimental study of stability, receptivity and transition of the flat-plate laminar boundary layer at Mach 3 are discussed. With a relatively low free-stream disturbance level ($\sim 0.1\%$), spectra, growth rates and amplitude distributions of naturally occurring boundary layer waves were measured using hot wires. Physical (mass-flux) amplitudes in the boundary layer and free stream are reported and provide stability and receptivity results against which predictions can be directly compared. Comparisons are made between measurements of growth rates of unstable high-frequency waves and theoretical predictions based on a non-parallel, mode-averaging stability theory and receptivity assumptions; good agreement is found. In contrast, it was found that linear stability theory does not account for the measured growth of low-frequency disturbances. A detailed investigation of the disturbance fields in the free stream and on the nozzle walls provides the basis for a discussion of the source and the development of the measured boundary layer waves. Attention is drawn to the close matching in streamwise wavelengths for instability waves and the free-stream acoustic disturbances. It was also found that a calibration of the hot wire in the free stream yields a double-peak boundary layer disturbance amplitude distribution, as has been found by previous investigators, which is not consistent with the predictions of linear stability theory. This double peak was found to be an experimental anomaly which resulted from assumptions that are frequently made in the free-stream calibration procedure. A single-peak amplitude distribution across the boundary layer was established only when the hot-wire voltage was calibrated against the mean boundary layer profile. Finally, the late stages of transition, at a higher Reynolds number with a higher free-stream disturbance level, were explored. Calibrated amplitude levels are provided at locations where nonlinearities are first detected and where the mean boundary layer profile is first observed to depart from the laminar similarity solution. A qualitative discussion of the character of ensuing nonlinearities is also included.

1. Introduction

Boundary layer transition from a laminar to a turbulent state has been theoretically and experimentally investigated for almost a century, motivated by the fact that friction and heat transfer characteristics change dramatically when transition from laminar to turbulent flow occurs. In supersonic and hypersonic flows, transition can have critical practical consequences since skin friction and aerodynamic heating play

† With an Appendix by A. V. Fedorov.

‡ Present address: General Electric Global Research, ES-206, One Research Circle, Niskayuna, NY 12309, USA.

a considerable role in vehicle design. The physical mechanisms leading to transition in high-speed flows are, however, still poorly understood (Reshotko 1994).

Early transition experiments in compressible flows (Dryden 1955) were aimed at investigating the effects of mean flow parameters on the transition Reynolds number. It was shown, at least qualitatively, that for low supersonic Mach numbers the movement of the location of transition, in response to a change in Mach number or in response to different heat transfer conditions at the wall, was consistent with predictions based on an asymptotic linear stability theory developed by Lees (1947). Later, the direct numerical solutions of the linear equations performed by Brown (1962) and particularly by Mack (see Mack 1984 for a comprehensive review of Mack's numerical work) revealed critical differences between stability in incompressible boundary layers and stability in the high-Mach-number compressible case, in particular the three-dimensionality as opposed to two-dimensionality of the most unstable first mode and the existence of higher unstable modes in the high-speed case.

A major impediment in conducting useful and reliable compressible boundary layer stability and transition experiments was (and still remains) the high level of free-stream disturbances characteristic of conventional wind tunnels (Reshotko 1994). A high level of free-stream disturbances is often responsible for a bypass of physical mechanisms which would otherwise occur in low-disturbance environments (e.g. instability growth and boundary layer receptivity to low-intensity external disturbances), preventing these mechanisms from being properly studied and documented. Discrepancies between measurements and theory, and scatter between data collected in different facilities, have for the most part been attributed to different levels and characteristics of free-stream noise (Laufer 1954; Morkovin 1957, 1959; Pate & Schueler 1969) or in some cases to difficulties with measurement techniques (Schneider 2001). To advance knowledge of receptivity mechanisms at high speeds, it is necessary to perform experiments in a low-disturbance environment and to document characteristics of the remaining free-stream disturbances such as the disturbance source, disturbance level, speed of propagation and disturbance spatial structure.

In general, the 'turbulence' in the free stream of a supersonic wind tunnel consists of the superposition of a vorticity mode, an acoustic mode and an entropy mode (Kovasznay 1953; Morkovin 1957). The predominance of any one of these classes of disturbances depends upon the design and construction of the facility as well as the operating flow conditions. Bushnell (1990) discusses sources of free-stream disturbances in wind tunnels. At high speed ($M > 2.5$), the dominant free-stream disturbance mode, for well-designed conventional facilities operated at relatively high unit Reynolds number conditions, is sound radiation originating from turbulent or transitional nozzle-wall boundary layers (Laufer 1961, 1964; see also discussion in Bushnell 1990 and Reed *et al.* 1997). Kendall in 1967 performed an experiment on a flat-plate boundary layer at Mach 4.5 in a wind tunnel facility operated at pressures low enough for the tunnel boundary layers to be laminar (Kendall 1967). In the absence of sound radiation from the wall boundary layers, the free-stream turbulence level was reduced to very low values ($< 0.05\%$). Controlled waves were then introduced in the laminar boundary layer by means of a glow discharge actuator. Measurements of spatial amplification rates and phase velocities showed excellent agreement with the numerical calculations by Mack (Kendall 1967) and confirmed unequivocally the applicability of compressible linear stability theory and the differences between the compressible and incompressible case. More recent experiments, aimed at investigating the evolution of naturally occurring instability waves in zero-

pressure-gradient laminar boundary layers were conducted by Kendall (1975), by Lebiga, Maslov & Pridanov (1979) and by Demetriades (1989). A number of experimental investigations have also been conducted to study stability and transition on round cones (Schneider 2001 has reviewed three of these contributions).

Only a few detailed experiments have been performed with the intent of examining nonlinear stability phenomena in compressible flows (e.g. Kimmel & Kendall 1990; Kosinov *et al.* 1994). For the most part, investigations in the nonlinear regime have been aimed at determining the effects of mean flow parameters (such as wall temperature, nose bluntness etc.) on the location of transition (e.g. Chen, Malik & Beckwith 1989). More has been accomplished theoretically. Secondary instability mechanisms in compressible boundary layer flows have been investigated recently by Masad & Nayfeh (1990), El-Hady (1992), Ng & Erlebacher (1992), and Chang & Malik (1994). Direct numerical simulations of transition in compressible flows have been carried out by several authors (e.g. Erlebacher & Hussaini 1990; Pruett & Zang 1992; Thumm, Wolz & Fasel 1989; Pruett & Chang 1993). In addition, methods based on the parabolized stability equations (PSE) have been applied to the study of linear and nonlinear spatial wave evolution in compressible flows (Pruett & Chang 1993).

In the present work, results are presented from a comprehensive study of the stability, receptivity and transition of a Mach 3 flat-plate boundary layer. Following Kendall (1967), the present experiments were conducted while operating the facility at low unit Reynolds number conditions in an attempt to achieve laminar nozzle boundary layers and consequently low-intensity free-stream fluctuations. Performing the experiment at a low unit Reynolds number condition has the further advantage of yielding a relatively thick laminar flat-plate boundary layer along a substantial length of the plate in which accurate measurements of amplitude distributions can be made. Also, the frequencies of the boundary layer disturbances are relatively low and well within the frequency response of the hot-wire sensor used for the measurements.

Emphasis has been placed on characterizing the free-stream disturbances, measuring the amplitude and development of naturally occurring linear instabilities and providing comparisons with theoretical predictions. Also, measurements were made, in the nonlinear regime, of both the disturbances and the mean boundary layer profile. Unlike most of the previous studies, calibrated disturbance amplitudes are provided which will allow direct comparisons with computational and future experimental investigations.

2. Experimental apparatus

2.1. *The LTVG wind tunnel*

The experiments have been carried out in the test section of the Low Turbulence Variable Geometry (LTVG) Mach 3 wind tunnel at Princeton University. A schematic of the facility is shown in figure 1. A system of ejectors is used to run the facility at low stagnation pressures (typically 4–5 p.s.i.a.).

A critical component of the tunnel is the stagnation chamber. It has a relatively large volume (figure 1) and was designed to provide attenuation of flow disturbances before the contraction section. A noise dampening metal cone and a rigimesh screen are utilized to attenuate the acoustic noise generated by the inlet valve, and a set of screens and honeycombs spanning the section of the stagnation chamber were used to reduce the characteristic length scale of free-stream turbulence. Vorticity fluctuations (free-stream turbulence) are further reduced by the long length of the settling chamber

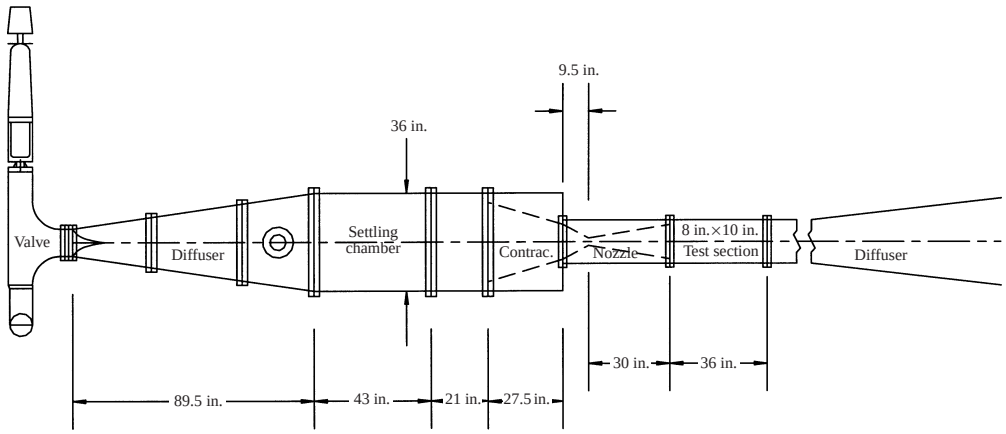

FIGURE 1. Schematic of the LTVG wind tunnel.

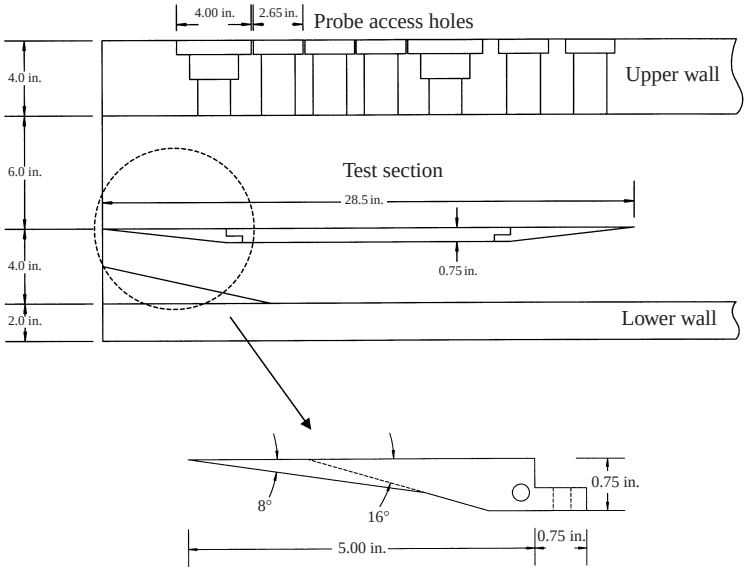

FIGURE 2. Outline of test section with the flat plate.

(approximately 15 ft) and by the large ratio of settling chamber cross-sectional area to sonic nozzle throat area (55 to 1) (Morkovin 1959).

2.2. *The flat plate and the traversing mechanism*

A brass flat plate, 28.5 in. long, was used for the experiments (figure 2). It has a 0.75 in. thick main body with removable tapered leading and trailing edge sections. The plate spanned the 8 in. wide test section and was positioned horizontally 2 in. below the centre-plane of the square nozzle (figure 2). Figure 2 shows that the flow is expanded underneath the plate to a test section height of 10 in. in order to partially compensate for the rise in static pressure through the shock waves below the plate leading edge. The leading edge of the plate was located at the joint between the nozzle and the test section. In order to minimize corner disturbances, and simultaneously guarantee the mechanical strength of the model, a double-tapered leading-edge design was adopted (figure 2). The trailing edge was also bevelled, in this case with an angle

P_0 (p.s.i.a.)	4.0 ($\pm$1%)	4.2 ($\pm$1%)	5.0 ($\pm$1%)
Re/in.	5.54×10^4 ($\pm$7%)	5.82×10^4 ($\pm$7%)	6.91×10^4 ($\pm$7%)
M	2.98 ($\pm$2%)	2.98 ($\pm$2%)	2.98 ($\pm$2%)
$\langle \rho u \rangle_{fs}/(\rho U)_{fs}$ ($1 < f < 40$ kHz)	0.11%	0.16%	0.39%

TABLE 1. Experimental operating conditions ($T_0 = 290$ K) and free-stream disturbance levels.

of 10°, to decrease total pressure loss and to reduce the size of the subsonic region in the aft wake where pressure disturbances can propagate upstream and interfere with the boundary layer flow over the plate. The working surface of the plate (main body, and leading and trailing edge assembled together) was ground to a finish of 4 corresponding to an r.m.s. roughness of about 4×10^{-6} in. The leading edge was checked regularly for imperfections and a uniform sharpness of about 0.5×10^{-3} in. (measured with a calibrated telescope) was maintained.

A traversing mechanism coupled to a stepper motor and mounted over the upper surface of the test section was used to move the probe in the vertical direction. Access to the flat-plate model in the test section was obtained through circular holes located on the centreline of the upper surface (figure 2). Probe bodies of different lengths permitted measurements at intermediate downstream stations along the plate. The stepper motor was driven by a software-controlled pulse generator and required 5000 pulses per inch of traverse. A calibrated potentiometer, connected to the A/D converter of the data acquisition system, was used to monitor the actual position of the traversing block. To minimize the transmission of vibrations from the wind tunnel to the probe driving mechanism, the latter was isolated from the test section with vibration damping pads.

2.3. *The data acquisition system*

A modular Camac System with $\pm$5 V input range was used for the acquisition of mean and fluctuating quantities. A Le Croy 8212A Fast Data Logger was used to sample all the mean quantities at 200 Hz, whereas a 4 channel Le Croy TD8210 Wave Form Analyzer, with adjustable sampling frequency (up to 1 MHz) and a resolution of 9.8 mV per count (10 bits), was utilized to acquire simultaneously (less than 5 ns uncertainty) the rapidly fluctuating hot-wire voltages.

3. Mean flow surveys and test conditions

Pitot-static surveys were made of the mean flow field along the centreline of the flat plate from approximately 3 in. to 13 in. downstream of the leading edge. The rectangular shape of the tip of the Pitot tube was obtained by flattening the tip of a 0.065 in. diameter stainless steel tube. The resulting probe dimensions were approximately 0.02 in. $\times$ 0.08 in. with a rectangular orifice 0.011 in.–0.013 in. high.

The initial y-position of the Pitot-static probe was measured with respect to the wall by utilizing a magnifying telescope provided with a calibrated scale. Because of the low dynamic loading at the flow conditions of the experiment, observations during runs showed that no significant probe deflection occurred. The error in determining the initial distance from the wall was found to be $\pm$0.002 in.

The experiments were mainly conducted at three values of the stagnation pressure as indicated in table 1. The free-stream Mach numbers, reported in the table,

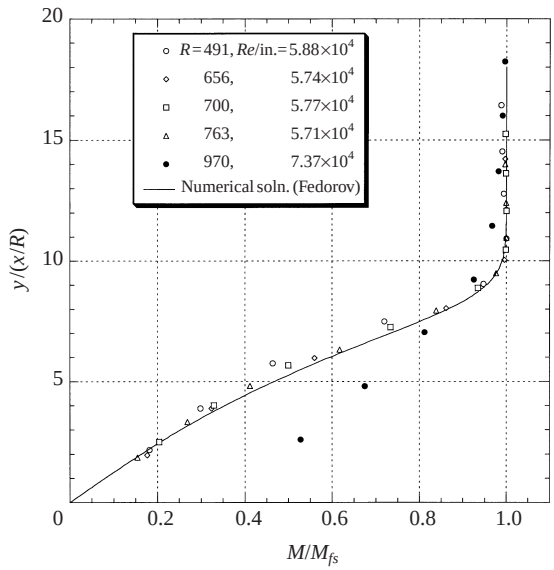

FIGURE 3. Mean boundary layer profiles. Pitot-static measurements vs. boundary layer calculations.

were measured 4 in. downstream of the leading edge along the plate centreline. Also included in the table is the measured free-stream disturbance level at each of these conditions (the brackets $\langle\ \rangle$ define the root-mean-square of the measured fluctuations).

Due to the short running time (80–100 s) and the thermal characteristics of the plate, the plate surface was determined to be virtually isothermal during the experiments with a wall temperature equal to 1.1 times the adiabatic temperature at the wall ($T_w = 1.1\ T_{aw}$).

3.1. *Mean boundary layer profile and transition Reynolds number*

Since the Mach number is obtained directly from measured pressure quantities, Mach number profiles were selected (as opposed to velocity or mass-flux profiles) to make comparisons with compressible boundary layer calculations.

The measured profiles along with the computed profile corresponding to the experimental conditions (A. V. Fedorov 2001, private communication) are plotted in similarity coordinates in figure 3. Good agreement is obtained between the measurements and the predictions except in the vicinity of the leading edge ($x < 5$ in., $R < 550$ ($R = Re_x^{1/2}$)) where probe interference effects due to the small boundary layer thickness δ ($\delta < 0.08$ in., $h/\delta > 0.25$ where h is the height of the probe) cause a spurious bulge in the mean profile for $4 < \eta < 9$ ($\eta = y/(x/R)$) and a small overshoot at the outer edge of the boundary layer ($R = 491$, figure 3). Also included in figure 3 is the transitional flat-plate boundary layer profile measured at $x = 12.75$ in. at the highest stagnation pressure, $P_0 \sim 5.0$ p.s.i.a. ($R = 970$). It is important to appreciate that transition was observed at a 'low' Reynolds number only at the highest stagnation pressure of 5 p.s.i.a. (for this case $R_{tr} \sim 800$, $Re_{x,tr} \sim 0.6$–0.7×10^6 and $Re/\text{in.} = 7.1 \times 10^4$). The reason is that the free-stream disturbance level measured at the plate leading edge was considerably higher than at 4 p.s.i.a. (table 1) and also that at the highest pressure the free-stream disturbance amplitude grew more rapidly in the streamwise direction downstream of the leading edge (figure 10) and finally that, as

determined from free-stream disturbance measurements (Graziosi 1999), transition on the upper-wall boundary layer causes a further increase of the free-stream disturbance level at approximately 9–10 in. downstream from the plate leading edge. Nonetheless, the transition Reynolds number determined at $P_0 \sim 5.0$ p.s.i.a. is comparable with measurements in conventional supersonic facilities reported by previous authors. In the AEDC tunnel D (12 in. $\times$12 in.), at $M = 3$, Beckwith & Miller (1990) report $Re_{x,tr} \sim 1.2$–1.3×10^6 measured at $Re/\text{in.} \sim 6 \times 10^5$ and $Re_{x,tr} \sim 1 \times 10^6$ measured at $Re/\text{in.} \sim 3 \times 10^5$. Also, from figure 3 in their article, where results corresponding to three conventional facilities are presented (JPL 20 in., tunnels A and D at AEDC), the measured flat-plate transition Reynolds number decreases with tunnel size and unit Reynolds number.

At $P_0 \sim 4.0$ p.s.i.a., with a low free-stream disturbance level of 0.11%, the boundary layer profiles collapsed to the laminar similarity profile down to approximately 12 in. from the leading edge. Further downstream, before transition occurred at this low stagnation pressure, the profile began to depart from the similarity solution, evidently due to a small local adverse pressure gradient (Graziosi 1999).

4. Hot-wire calibration and mass-flux amplitude distributions across the boundary layer

4.1. *Hot-wire technique: operation, data acquisition and reduction*

Small custom-made hot-wire probes manufactured by Auspex, Inc. were employed in order to measure the disturbances in the free stream and in the boundary layer. Simultaneous, dual-probe measurements were performed to determine streamwise and spanwise flow correlations in the free stream. In order to minimize probe interference effects for measurements in the boundary layer, the main body of the hot-wire probe was inclined at an angle of approximately 45° with respect to the plate surface and it remained outside the boundary layer during the measurements.

The sensor was a tungsten filament, 2.75×10^{-4} in. in diameter and approximately 0.04 in. long. The hot-wire probes were used in conjunction with Dantec constant-temperature anemometers (model DISA 55M01 Main Unit and DISA 55M12 Bridge Circuit). Typical hot-wire frequency responses of approximately 120 kHz were obtained by a standard square-wave method. At a constant wire temperature, the hot-wire output in supersonic flow is typically assumed to be sensitive to mass-flow fluctuations and total temperature fluctuations. In order to maximize the frequency response and simultaneously reduce the total temperature sensitivity, the hot wire was operated at the relatively high overheat ratio τ of 0.7 to 0.8 ($\tau = (T_w - T_r)/T_0$, where T_w is the wire temperature, T_r the recovery temperature at the wire and T_0 the total temperature).

The length of the sampled time series of the hot-wire voltage was selected according to the lowest frequency component of interest. Frequencies above 1 kHz were quantitatively examined in the present study, and thus sequences for a period of at least 200 ms were recorded at a sampling rate of 250 kHz. The time signals were then processed to yield the spectra of the fluctuations. Standard techniques such as partitioning of the original data sample were employed to minimize the standard deviation of the power estimate (Press *et al.* 1992). Power spectral estimates and cross-correlations were evaluated using different segment lengths and different numbers of segments with fixed length. The results showed that a choice of 48 partitions with a partition length of 1024 points would yield convergence of the energy estimates for a

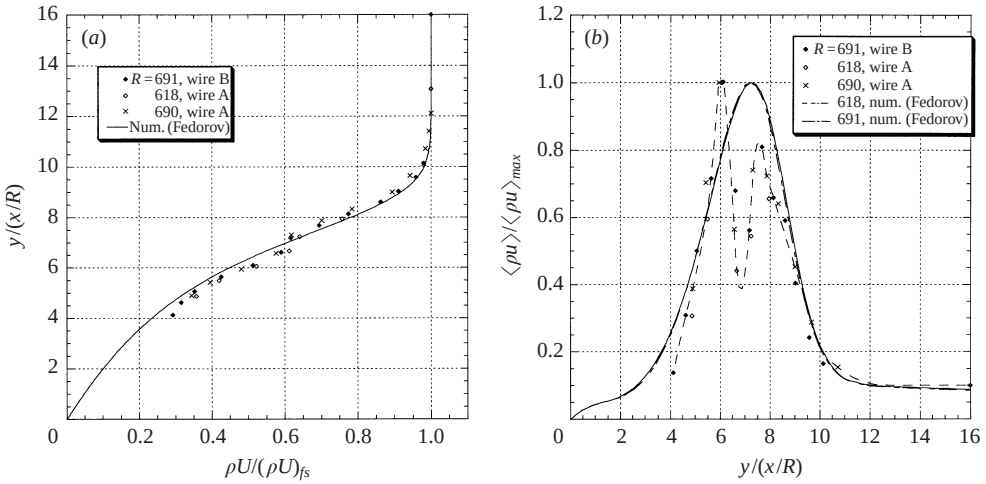

FIGURE 4. (*a*) Mean boundary layer profiles, hot-wire measurements vs. boundary layer calculations; (*b*) measured r.m.s. mass-flux amplitude distributions (free-stream calibration) vs. computed eigenfunction (Fedorov). $F = 5.0 \times 10^5$, $Re/\text{in.} = 5.51 \times 10^4$.

number of narrow frequency bands 1.4 kHz wide (within 2% for frequencies greater than 2 kHz). In order to minimize the problem of power 'leakage' from adjacent frequency components, the discrete data segment was multiplied by a proper time window ('Welch window') before the FFT was computed (Press *et al.* 1992).

4.2. *Free-stream versus boundary layer hot-wire calibration and determination of the y-distribution of the mass-flux disturbance amplitude*

In supersonic flows, the hot wire is usually calibrated in the steady free stream of the wind tunnel by changing the stagnation pressure at a fixed Mach number. It is common practice to use the following non-dimensional form of King's law to reduce the data points to an analytical form:

$$Nu_0 = X + Y\,Re_0^n \tag{4.1}$$

(the subscript 0 indicates that the fluid properties are evaluated at the stagnation conditions). For a given wire and a constant Prandtl number, X and Y are functions solely of the overheat ratio; in particular they are assumed to be independent of Mach number in the range $1.2 < M < 5$ and for a wire Reynolds number Re_0 greater than 20 (Smits, Hayakawa & Muck 1983). A free-stream calibration and King's law were employed in the present experimental investigation to yield the values of the hot-wire sensitivities and thus the r.m.s. mass-flux amplitudes in the free stream (despite the low value of $Re_{0,fs} = 6.5$–7).

Despite the fact that the above conditions for the Mach number and wire Reynolds number were typically not met across the compressible boundary layer, and that the stagnation pressure could not be lowered enough during the calibration runs to safely interpolate all the data points taken in the boundary layer, a free-stream calibration and King's law were initially employed to determine mass-flux amplitude distributions across the boundary layer.

Typical laminar boundary layer mean profiles obtained with two different hot-wire sensors, calibrated in the free stream, are shown in figure 4(*a*) along with the numerical calculations of the boundary layer (A. V. Fedorov 2001, private communication). The

surveys do not extend to the wall region since the supersonic free-stream calibration obviously breaks down in the subsonic portion of the boundary layer. The overall agreement between the hot-wire measurements and the numerical predictions might be considered satisfactory; however a careful examination of the figure reveals the systematic occurrence of a 'knee' in the hot-wire profile at a value of $\rho U/(\rho U)_{fs} \approx 0.6$ (at a corresponding value of the similarity coordinate η of approximately 7). This discontinuity seemed most likely to be a spurious result of the hot-wire measurement technique rather than an abnormality of the boundary layer flow. This was confirmed by the Pitot measurements displayed in figure 3. It was confirmed also, by visual inspection through a high-resolution telescope, that no significant prong and/or wire deflection, which might account for the 'knee' in the mean profile, occurred during a hot-wire boundary layer survey.

Figure 4(*b*) shows the corresponding narrow frequency band fluctuation amplitude profiles obtained with the free-stream calibration of the hot wires. The selected non-dimensional frequency, $F = 5.0 \times 10^{-5}$ where $F = 2\pi\nu f/U_{fs}^2$, corresponds approximately to the most unstable boundary layer linear mode for the explored range of Reynolds number R. The predicted eigenfunction is also included in figure 4(*b*) ($M = 2.98$, $T_w = 1.1\,T_{aw}$) (A. V. Fedorov 2001, private communication). A broad range of spanwise modes has been included in the theoretical stability model as discussed in the Appendix and § 6.2. It is immediately apparent from figure 4(*b*) that the measured amplitude distribution is distinguished by a double hump shape which is not predicted by the linear stability calculations (the corresponding measured r.m.s. voltage profile is also characterized by a double peak). Previous authors have also observed the occurrence of double-peak amplitude distributions across a flat-plate boundary layer at Mach 3 (e.g. Kendall 1975).

By comparing figure 4(*a*) and figure 4(*b*), it is evident that the region between the two peaks in the amplitude distribution corresponds to the region where the 'knee' in the mean profile occurs.

The hot-wire data of Laufer & Vrebalovich (1960) at a Mach number of 2.2 display a similar feature for both the mean profile and mean-square voltage profile. The y-location of the knee in the measured mean profile (figure 15 in Laufer & Vrebalovich 1960) also corresponds closely to the region of the trough between the two peaks in the mean-square voltage profile (figure 17 in Laufer & Vrebalovich 1960). Laufer & Vrebalovich (1960) suggest that the outer peak in the r.m.s. voltage distribution could be the result of an anomalous hot-wire response since, during their experiment, the double-peak distribution was observed only for high values of the overheat ratio.

To clarify the cause of the double-peak distribution for the results in figure 4(*b*), it was decided to calibrate the hot-wire mean voltage measured across the boundary layer directly against the mean mass-flux boundary layer profile (figure 3). Calibration curves (mean hot-wire voltage versus mean boundary layer mass-flux normalized by the corresponding free-stream values) obtained by means of this boundary layer calibration are displayed in figure 5(*a*). Figure 5(*b*) shows the mass-flux sensitivity distributions for the two hot-wire sensors used for the measurements of figures 4 and 5(*a*). The sensitivity distributions were determined by differentiating smooth curves fitted through each of several calibration curves measured in the similarity region of the boundary layer flow (a sample is shown in figure 5*a*) and by taking the average of the derivatives at several locations across the boundary layer. It is interesting to note that a relatively flat region characterizes the calibration curves for $0.55 < \rho U/(\rho U_{fs}) < 0.65$. A corresponding dip in the sensitivity curves (at $\eta \sim 7$) can be seen in figure 5(*b*).

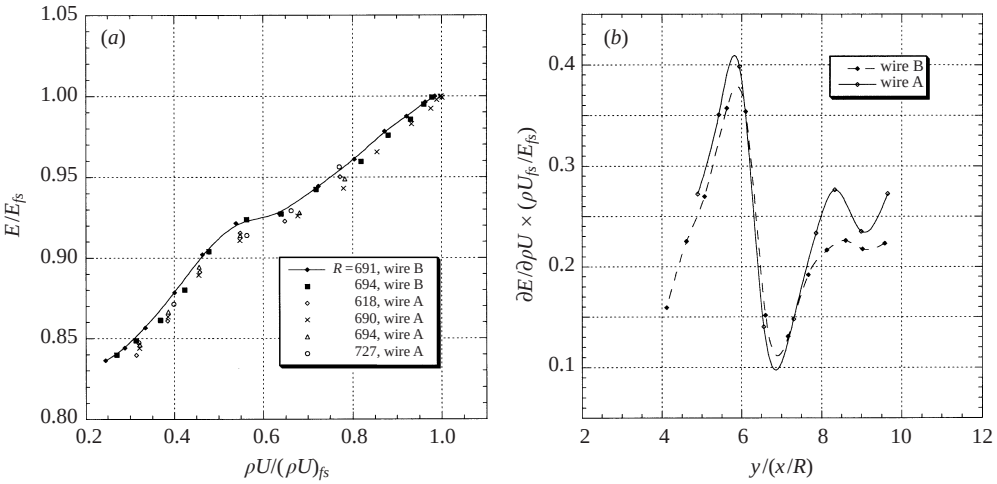

FIGURE 5. (*a*) Hot-wire boundary layer calibration curves, (*b*) hot-wire mass-flux sensitivity distributions. $Re/\text{in.} = 5.51 \times 10^4$.

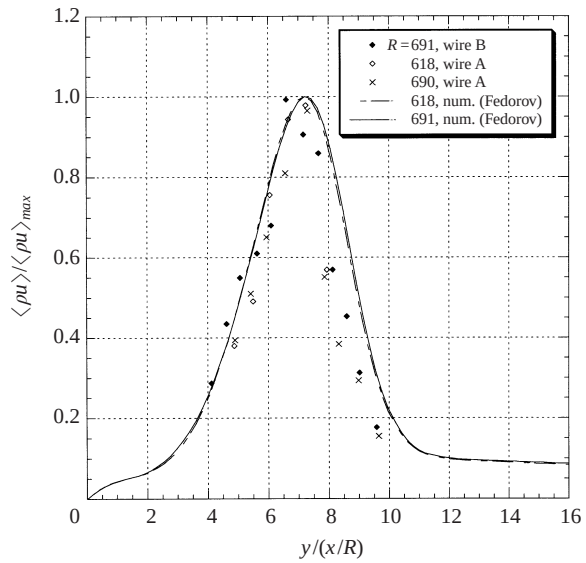

FIGURE 6. Measured r.m.s. mass-flux amplitude distributions (boundary layer calibration) vs. computed eigenfunction (Fedorov). $F = 5.0 \times 10^5$, $Re/\text{in.} = 5.51 \times 10^4$.

The 'knee' in the mean profiles of figure 4(*a*) and the trough between the two peaks in the corresponding r.m.s. voltage amplitude distributions of figure 4(*b*) can be explained as a result of this region of low wire sensitivity in the central portion of the boundary layer (they occur at exactly the same η as where the dip in the sensitivity distributions of figure 5*b* occurs). Note that the hot-wire sensitivities (and consequently the disturbance amplitudes) could not be reliably determined from the boundary layer calibration for $\eta \geqslant 10$: at the outer edge of the boundary layer, due to the small mean mass-flux gradient, a large scatter in the computed sensitivities was observed.

The r.m.s. mass-flux distributions which result from the boundary layer calibration of the hot wires are shown in figure 6. As is apparent, the boundary layer calibration

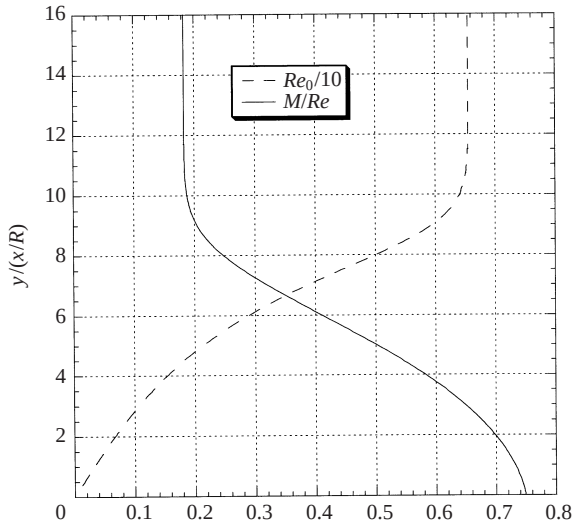

FIGURE 7. Re_0 and M/Re distributions across the laminar boundary layer. $Re/\text{in.} = 5.51 \times 10^4$.

yields single-peak distributions which are consistent with the predicted amplitude distributions. The reasons for the remaining quantitative discrepancy between measurements and predictions in the outer part of the boundary layer need further investigation.

The behaviour of the calibration curve across the boundary layer (figure 5*a*) and the corresponding dip in the sensitivity distribution (figure 5*b*) appears to be a result of the complexity of the low-Reynolds-number supersonic flow field around the wire. The heat transfer from the hot-wire sensor, and so the Nusselt number, depends in general on a large number of parameters such as the Reynolds number based on the wire diameter, the Prandtl number, the Mach number, the Knudsen number Kn, the overheat ratio and the physical properties of the sensor (for a detailed discussion see Hinze 1975). Whenever the flow departs from the continuum condition ($Kn > 0.01$), the Mach number is expected to enter the problem indirectly through the Knudsen number and Reynolds number (since $M \sim Kn\,Re$).

Figure 7 shows the calculated profiles of the Reynolds number ($Re_0/10$) and M/Re ($\sim Kn$) across the boundary layer for typical experimental conditions ($P_0 =$ 4.0 p.s.i.a., $T_0 = 290.5$ K, $T_w = 1.1\,T_{aw}$). It is apparent from figure 7 that, for the present case, the Nusselt number dependence on the Mach number could be significant because of the high values of the Knudsen number and correspondingly low values of Re_0 across the boundary layer. It is interesting to note that the region of low wire sensitivity (figure 5*b*) and the corresponding 'knee' in the distribution of the mean voltage across the boundary layer (figure 5*a*) occur for a 'transitional' value of the Knudsen number of approximately 0.32 and a local Mach number of ~ 2.2 at $P_0 \sim 4.0$ p.s.i.a. ($Re/\text{in.} = 5.51 \times 10^4$). (Interestingly, since the thickness of a shock is of the order of 5 times the mean free path, at these conditions a shock would have a thickness of the order of the wire diameter). Results obtained at a different pressure, namely 5 p.s.i.a., showed that the sensitivity distribution was changed as a result of the changed distribution of wire Reynolds number.

Finally, we examined the fact that across the boundary layer the hot wire is sensitive to mass-flux fluctuations as well as Mach number fluctuations (the total

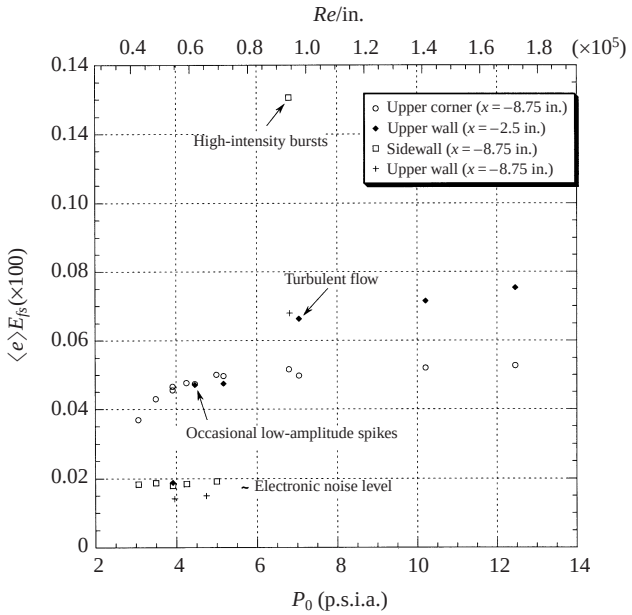

FIGURE 8. Hot-film r.m.s. voltage amplitudes measured at several locations on the nozzle walls.

temperature sensitivity is neglected due to the high overheat ratio at which the hot wire was operated, § 4.1) and that $\mathrm{d}M/\mathrm{d}\rho U$ evaluated for the mean profile is different from the ratio of the Mach number amplitude to the mass-flux amplitude across the boundary layer ($M'/\rho u'$). Since in the region of the measurements ($\eta > 4$), however, the difference between $\mathrm{d}M/\mathrm{d}\rho U$ and $M'/\rho u'$ is small (A. V. Fedorov 2002, private communication), we do not expect this difference to significantly affect the amplitudes determined with a boundary layer calibration of the hot wire.

5. Free-stream disturbances

All the measurements reported in this section were performed with the plate installed in the test section. The x, y, z coordinates reported on the figures are the streamwise, normal and spanwise coordinates respectively. The origin of the reference system is located at the mid-span of the flat-plate leading edge (figure 12).

5.1. *Corner disturbances as sources of free-stream fluctuations*†

In order to investigate the source and nature of the residual free-stream disturbances, hot-film measurements (not calibrated) were made on the centreline of the upper and side nozzle walls, and near the geometrical corner between the upper wall and the sidewall (on the sidewall, 0.25 in. from the corner line) at two axial locations along the nozzle (figure 12) and over a range of unit Reynolds numbers. The hot-film sensors consisted of a 0.06 in. long and 0.02 in. wide platinum strip coated with quartz, and yielded typical frequency responses of the order of 130–150 kHz as determined by the standard square-wave method.

At $x = -2.5$ in., the hot-film r.m.s. voltage, measured on the centreline of the upper wall at $P_0 \sim 4.0$ p.s.i.a., is comparable to the electronic noise level (figure 8). Also, for

† The authors are grateful to Dr J. Kendall for drawing their attention to corner disturbances as a possible source of free-stream disturbances.

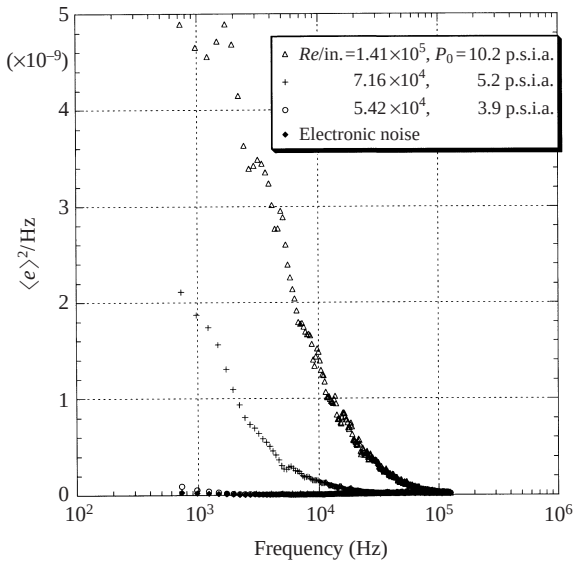

FIGURE 9. Spectra of the hot-film voltage fluctuations measured on the centreline of the upper nozzle wall. $x = -2.5$ in.

$f > 2$ kHz, the corresponding spectrum of the fluctuations is virtually coincident with the spectrum of the electronic noise (figure 9). These results confirm the absence of any significant flow disturbances and laminar flow. At the same location, as the stagnation pressure is increased to 4.5–5 p.s.i.a., a significant increase in hot-film r.m.s. voltage is measured (figure 8). At a stagnation pressure of approximately 7 p.s.i.a., the r.m.s. voltage reaches a value which is approximately equal to 3.5 times the 'undisturbed flow' value (in addition the time traces of the hot-film voltage – not reported – begin to exhibit a turbulent character).

The results in figure 8 also show that up to $P_0 \sim 5.0$ p.s.i.a., the disturbance level measured on the centreline of the upper and side walls at $x = -8.75$ in. is comparable with electronic noise (correspondingly, the spectrum of the fluctuations matches the spectrum of the electronic noise for $f > 2$ kHz) providing evidence that the boundary layers are laminar at this location and at pressures up to $P_0 \sim 5.0$ p.s.i.a. ($Re/\text{in.} \sim 7 \times 10^4$). At a stagnation pressure of approximately 7 p.s.i.a., the r.m.s. hot-film voltage, measured on the sidewall boundary layer at $x = -8.75$ in., increases by a factor of 7 with respect to the 'laminar' value (figure 8), indicating that transition is occurring (correspondingly high-intensity bursts are observed in the time traces of the disturbance signal – not reported). Also, at approximately 7 p.s.i.a. and at $x = -8.75$ in., the r.m.s. voltage measured on the upper-wall centreline increases to a value which is approximately 4.5 times the laminar value.

By contrast the disturbance level measured at $x = -8.75$ in. by the corner sensor is significant even at a low stagnation pressure of approximately 3 p.s.i.a. and the corresponding hot-film r.m.s. voltage slowly increases as the stagnation pressure increases above 3 p.s.i.a. (figure 8). Not surprisingly, the corner flow exhibits a disturbed character at a Reynolds number below the Reynolds number at which undisturbed flow is measured on the upper and side wall centreline. Lin *et al.* (1996) have conducted a computational study of the inviscid instabilities of the corner flow in a Mach 2.4 slow-expansion square nozzle. They found that spanwise cross-flow towards the corner

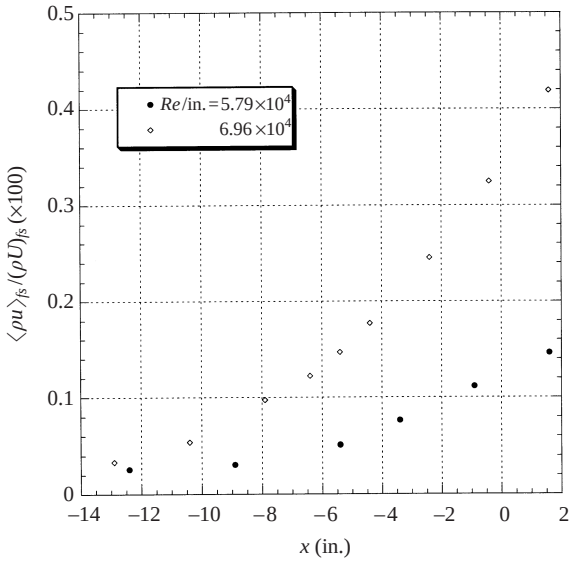

FIGURE 10. Free-stream r.m.s. mass-flux amplitudes measured along the centreline of the nozzle.

line in the convex region of the nozzle induces counter-rotating streamwise vortices at the corner. These vortical structures produce an inflectional streamwise velocity profile along the corner bi-sector plane (Lin *et al.* 1996). Balachandar & Malik (1995) performed a one-dimensional viscous stability analysis of the incompressible, inflectional bi-sector profile along a streamwise corner. The analysis yielded $R_{cr} \sim 21$ which is more than an order of magnitude lower than the critical Reynolds number of the Blasius profile ($R_{cr} \sim 300$) (Balachandar & Malik 1995). No quantitative comparisons between the results of the present study and the results in Lin *et al.* (1996) and Balachandar & Malik (1995) can be made. However, an order-of-magnitude extrapolation of the computational findings suggests that the corner flow, in the present Mach 3 case, may become unstable in the nozzle throat region at a unit Reynolds number well below the lowest unit Reynolds number of the investigation ($Re/\text{in.} \sim 5.5 \times 10^4$). Unlike the sidewall case, no high-intensity turbulent bursts were observed in the time traces of the hot-film voltage measured in the corner and on the upper wall for the explored range of unit Reynolds numbers ($Re/\text{in.} = 4 \times 10^4$–$1.8 \times 10^5$).

The results in figure 10 show that the broad-band free-stream disturbance level, measured with a hot wire along the nozzle centreline, increases with streamwise distance in the tunnel at a given stagnation pressure. In addition, the growth rate of the disturbances is evidently substantially larger at the higher stagnation pressure of approximately 5 p.s.i.a. ($Re/\text{in.} = 6.96 \times 10^4$). The calibrated amplitude measurements in figure 10 were collected in an early stage of the experimental investigation and before the hot wire had been properly tuned for high-frequency response. In this case the frequency response was cut off at approximately 15 kHz but it was, nevertheless, still above the frequency of the most energetic free-stream disturbances (figure 13). In addition, the data reported in figure 10 have not been corrected for electronic noise. Finally, we note that the acoustic origin of the most-downstream measurements in figure 10 ($x \sim 1.5$ in.) is approximately located on the nozzle walls at $x \sim -9.5$ in., upstream of the location ($x = -8.75$ in.) where undisturbed flow was measured on the centreline of the upper and side walls up to $P_0 \sim 5.0$ p.s.i.a. (figure 8).

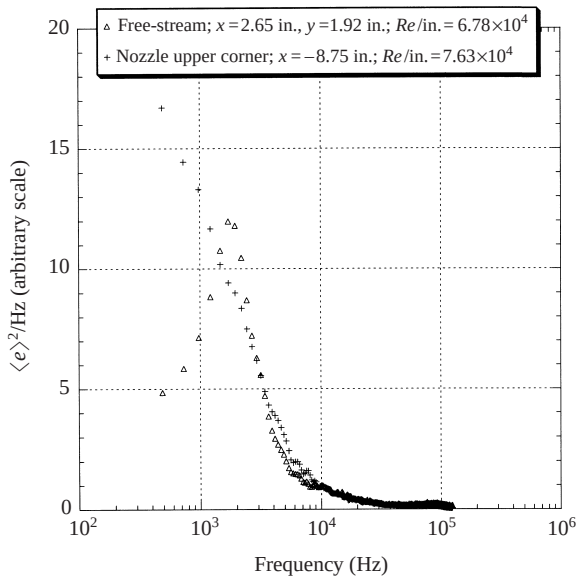

FIGURE 11. Spectra of the voltage fluctuations measured in the upper corner of the nozzle wall (hot film) and in the free stream (hot wire).

The monotonic increase of the free-stream disturbance amplitude with x inside the nozzle, the observed Reynolds-number dependence of the disturbance level at a given x (figure 10), the results of the hot-film measurements on the nozzle walls discussed above (figure 8) and the resemblance of the shape of the free-stream disturbance spectrum to the spectrum of the corner flow disturbances measured at the corresponding acoustic origin ($P_0 \sim 5.0$ p.s.i.a., figure 11) provide strong evidence that the free-stream disturbances, along the nozzle centreline, in the region of the leading edge of the plate (down to $x = 2.5$–3 in.) and at stagnation pressures up to $P_0 \sim 5.0$ p.s.i.a., are primarily the result of acoustic radiation from nozzle corner disturbances which develop in the downstream direction (figure 12). In addition, the very low free-stream disturbance level measured well inside the nozzle at $x \sim -13$ in. (figure 10) (less than 0.05% which is a value comparable to the disturbance level measured under quiet operation in the test rhombus of the NASA Mach 3.5 pilot quiet tunnel, Beckwith *et al.* 1983) rules out significant vorticity disturbances propagating from the stagnation chamber and provides further evidence of the acoustic nature of the measured free-stream fluctuations in the test section.

Additional detailed free-stream measurements were also made downstream from the leading edge to $x \sim 11.5$ in. along the centreline of the plate (Graziosi 1999). These measurements show that at the lower and intermediate unit Reynolds number conditions ($P_0 \sim 4.0$ and 4.2 p.s.i.a.) and at approximately 9.5 in. downstream of the leading edge, a significant relative increase in the energy of high-frequency components (6–20 kHz) occurs. The acoustic origin of these measurements on the sidewalls corresponds approximately to the x-location of the plate leading edge. With reference to figure 12, we conclude that, at $P_0 \sim 4.0$ p.s.i.a., the region of the flow, defined by Mach lines, where nozzle corner-flow disturbances are the primary source of free-stream disturbances, extends to 9–10 in. from the plate leading edge (along the plate centreline).

f(kHz)	1	3	10.5	17
$\lambda_{x,fs}$ (in.)	15.43	5.14	1.47	0.91
$\lambda_{x,BL}$ (in.) ($R = 500$)	N/A	4.79	1.48	0.98
$\lambda_{x,BL}$ (in.) ($R = 1000$)	12.68	4.84	1.61	1.09

TABLE 2. Streamwise wavelengths of free-stream disturbances (measured) and most unstable first-mode waves (calculated – Balakumar). $Re/\text{in.} = 5.51 \times 10^4$.

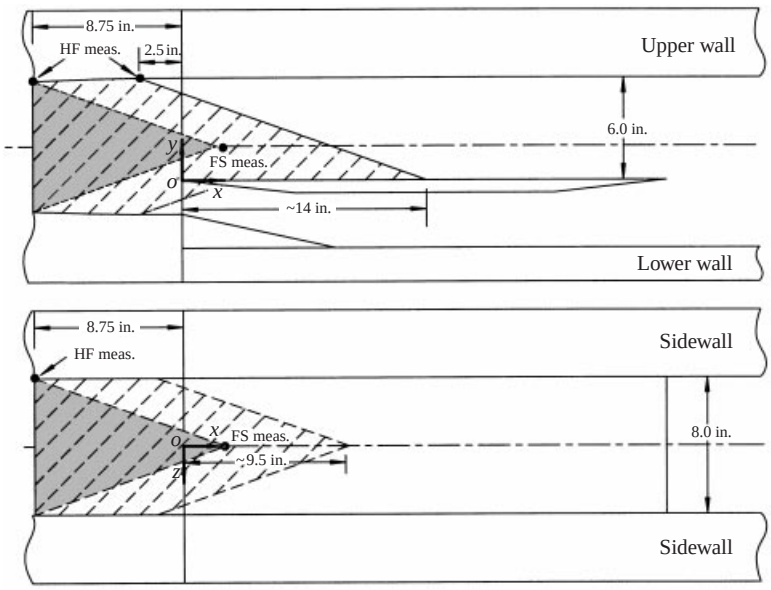

FIGURE 12. Regions of the flow where corner disturbances are the primary source of free-stream disturbances. Hatched: $P_0 \sim 4.0$ p.s.i.a. Shaded: $P_0 \sim 5.0$ p.s.i.a.

5.2. *Frequency content and spatial characteristics of the free-stream disturbance field*

The spectra of the free-stream mass-flux fluctuations measured with a hot wire 2.65 in. downstream of the leading edge, approximately on the centreline of the tunnel, are shown in figure 13 for the three unit Reynolds numbers of the experiments. Also shown in figure 13 is the unstable frequency range at $R = 400$, for a zero-pressure-gradient Mach 2.98 boundary layer, as predicted by parallel linear stability theory for adiabatic wall conditions (P. Balakumar 1998, private communication). The free-stream disturbance levels measured with a calibrated hot wire at $x = 3.03$ in., $y = 0.67$ in., $z = 0$ in. and corrected for the electronic noise (by subtracting the squares of the signals and taking the square root of the result), are reported in table 1. The low-frequency cutoff value of 1 kHz was selected for the free-stream measurements due to the significant contribution of tunnel and probe vibrations to the measured spectrum below a frequency of approximately 700–900 Hz. Correspondingly, the contribution of actual flow fluctuations at these low frequencies could not be easily extracted from the measured spectrum. Note that the inferred wavelength of a 1 kHz free-stream disturbance is approximately 15.5 in. (table 2) and the corresponding value of λ/δ at $R \sim 470$ is large (~ 220). Also, this cutoff frequency is one order of magnitude lower than the frequency of the most unstable first-mode wave for this boundary layer ($f \sim 10$ kHz, § 6.1).

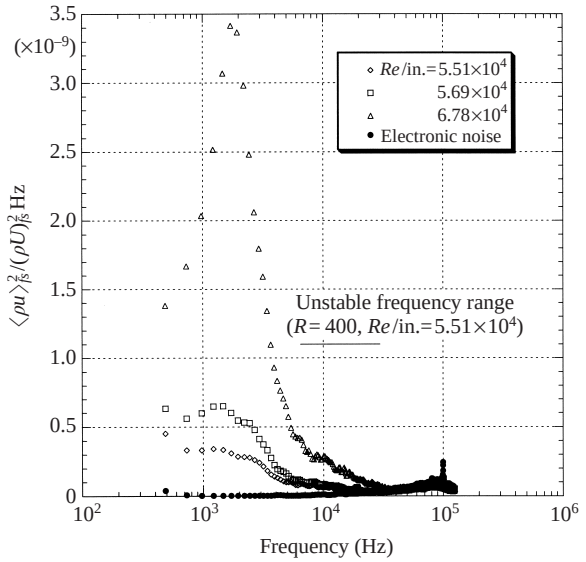

FIGURE 13. Spectra of the free-stream mass-flux fluctuations at different unit Reynolds number conditions. $x = 2.65$ in., $y = 1.92$ in.

Electronic noise contributes significantly to the free-stream measurements at frequencies above a value of approximately 10 kHz and noise accounts for the entire measured energy at frequencies higher than approximately 25 kHz and 40 kHz respectively for the lowest and highest unit Reynolds number cases in figure 13. Note that at $P_0 \sim 4.0$ p.s.i.a. the free-stream fluctuation level of 0.11% is higher than the quiet tunnel measurements (in the quiet core) by Beckwith *et al.* (1983) and the JPL measurements by Kendall (1967) with laminar wall boundary layer conditions (values of the order of 0.03% to 0.05%), but is much lower than the turbulence levels typically measured in conventional supersonic wind tunnels (up to 1%). In addition, as is apparent from figure 13, at the lowest and intermediate unit Reynolds number, most of the energy is at frequencies below 5 kHz, below the unstable linear range, and its magnitude increases considerably as the unit Reynolds number increases from 5.51×10^4 to 6.78×10^4.

In order to investigate the spatial structure of the free-stream disturbances and determine the speed of propagation, dual hot-wire measurements were made in the free stream and the phase and coherence functions were studied. The phase and coherence functions are defined respectively as the phase and the normalized amplitude squared of the average cross-spectrum of the two hot-wire signals:

$$\phi_i^{1,2} = \arg(H_i^1 H_i^{2^*}), \tag{5.1}$$

$$C_i^{1,2} = \frac{\left|H_i^1 H_i^{2^*}\right|^2}{\left|H_i^1\right|^2 \left|H_i^2\right|^2}, \tag{5.2}$$

where H_i^1 and H_i^2 are the complex Fourier coefficients corresponding to the frequency component i of the digital Fourier transforms of the two hot-wire fluctuating voltages. ($C_i^{1,2} = 1$ indicates perfect correlation between the hot-wire signals at the frequency i).

Unlike the amplitude, the phase characteristics of the free-stream disturbances, measured in a region close to the leading edge (figures 14 and 15), were found in

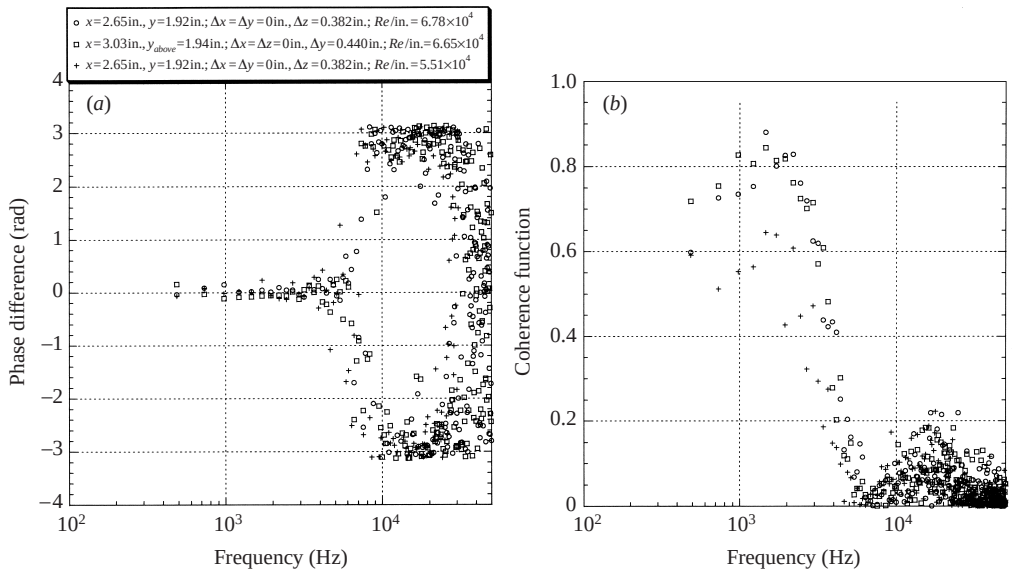

FIGURE 14. (*a*) Phase and (*b*) coherence functions measured in the free stream.

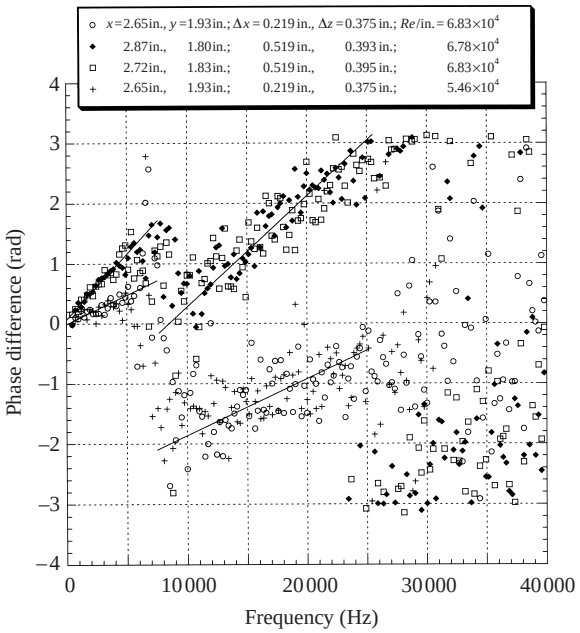

FIGURE 15. Phase function measured in the free stream with two hot wires displaced in both *x*- and *z*-directions.

the experiments not to depend significantly on the unit Reynolds number (at least within the explored range). This result is consistent with the fact that, as argued in § 5.1, remaining corner disturbances are the main source of free-stream disturbances, at the location of the measurements, up to the highest stagnation pressure of 5 p.s.i.a. (figure 12).

Figure 14 displays the phase (*a*) and coherence (*b*) functions obtained with two hot wires displaced in the spanwise (*z*) direction and in the transverse (*y*) direction

respectively. The measurements were made downstream of the plate leading edge ($x \sim 2.5$–3 in.) approximately on the centreline of the tunnel (above the Mach line originating at the plate leading edge) at $P_0 \sim 5.0$ and ~ 4.0 p.s.i.a. The results show a symmetric pattern in the z- and y-directions. Note that in both cases the phase difference is essentially zero for $f < 5$ kHz and π for $f > 9$ kHz. The transition from 0 to π occurs quite abruptly in a range of frequencies $5 < f < 9$ kHz. The coherence function (which is a measure of the degree of correlation as a function of frequency) exhibits a large broad peak (~ 0.8–0.9 at $P_0 \sim 5.0$ p.s.i.a. and ~ 0.65 at $P_0 \sim 4.0$ p.s.i.a.) at low frequencies ($f \sim 2$ kHz) followed by a decrease to zero in a range of frequencies corresponding to the range where the phase jump occurs. As the frequency increases further ($f > 9$ kHz), an additional modest peak (~ 0.2) emerges in the coherence function ($f \sim 15$–20 kHz) followed by a decrease to zero in a range of frequencies where free-stream disturbances do not contribute significantly to the energy of the signal ($f > 30$ kHz).

A simple mathematical model was developed in order to qualitatively interpret the results of the measurements of the free-stream phase and coherence functions. Acoustic radiation from the four nozzle corners is modelled by four conical travelling waves originating at the corners. Because of the square nozzle section, the resulting acoustic field would be symmetrical relative to the centreline of the duct. We approximate these waves as locally plane waves and consider four monochromatic components such that

$$h_{i1} = A\cos(k_x^i x + k_y^i y + k_z^i z - \omega t + \varphi_i) \tag{5.3}$$

where

$$\begin{aligned} k_x^1 &= k_x^2 = k_x^3 = k_x^4 = k_x, \\ k_y^1 &= -k_y^2 = -k_y^3 = k_y^4 = k_y, \\ k_z^1 &= k_z^2 = -k_z^3 = -k_z^4 = k_z \end{aligned}$$

(for simplicity, equal amplitudes are assumed). The phase fronts of these plane waves are inclined at opposite angles relative to the streamwise direction and give rise to a symmetric acoustic field with respect to the centreline of the duct.

We now compute the time cross-correlation between the output signals of two sensing elements which are displaced in the spanwise (z) direction and immersed in the flow field of four such waves. We assume that $h_1(x, y, z, t)$, $h_2(x, y, z, t)$, $h_3(x, y, z, t)$ and $h_4(x, y, z, t)$ are not correlated in phase (as would be the case for random disturbances). The component $h_i(x, y, z, t)$ contributes to the cross-correlation as

$$C_i(\tau) = \frac{1}{T}\int_0^T h_i(x, y, z, t)\, h_i(x, y, z + \Delta z, t + \tau)\, \mathrm{d}t,$$

where Δz is the distance between the sensors. Substituting the expression for $h_i(x, y, z, t)$ in the above integral yields

$$C_i(\tau) = \frac{A^2}{2}\cos(k_z^i \Delta z - \omega\tau).$$

Thus, the correlation coefficient is

$$\frac{C(\tau)}{2A^2} = \sum_i \frac{C_i(\tau)}{2A^2} = \cos(k_z \Delta z)\cos(\omega\tau). \tag{5.4}$$

Note that regardless of the value of Δz and the spanwise wavelength of the disturbance

($\lambda_z = 2\pi/k_z$), the time correlation will either have a maximum ($\cos(k_z\Delta z) > 0$) or a minimum ($\cos(k_z\Delta z) < 0$) at $\tau = 0$. For a fixed Δz, as the frequency increases the components of the wave vector will increase and the amplitude of the correlation coefficient in equation (5.4) (and therefore the coherence as determined from equation (5.2)) would monotonically decrease from a value equal to one (for $k_z = 0$) to a value equal to zero as $k_z\Delta z \to \pi/2$. Correspondingly, the phase difference will be zero in the range $0 < k_z\Delta z < \pi/2$. As the frequency (and the wavenumbers) increases further ($\pi/2 < k_z\Delta z < \pi$) the amplitude of the correlation coefficient will now increase monotonically from zero and the phase will change to π. The frequency at which the phase jump will occur is a function of the spacing Δz between the sensing elements and corresponds to the value at which the amplitude of the correlation coefficient goes to zero. Similarly, because of the assumed symmetry, the correlation between the signals of two sensors displaced in the y-direction is obtained by replacing z and Δz with y and Δy in equation (5.4). In figure 14, the value of the peak of the measured coherence function at $f \sim 15$–20 kHz is smaller than the value of the peak at the lower frequency of ~ 2 kHz due presumably to the smaller characteristic lengths of the disturbances with respect to the sensor spacing.

The model can be used to estimate locally, on the centreline of the duct, the spanwise (z) and transverse (y) wavelengths for the free-stream disturbances at a frequency of approximately 7 kHz where the phase jump occurs (figure 14). We find

$$\lambda_z(\tilde{f}) = 4\Delta z \approx 1.5\,\text{in.}, \quad \lambda_z(\tilde{f})/\delta \approx 21, \quad \tilde{f} \approx 7\,\text{kHz},$$
$$\lambda_y(\tilde{f}) = 4\Delta y \approx 1.8\,\text{in.}, \quad \lambda_y(\tilde{f})/\delta \approx 25, \quad \tilde{f} \approx 7\,\text{kHz},$$

where δ is the value of the boundary layer thickness measured on the plate leading edge at $x = 3.5$ in.

To determine the streamwise speed of the free-stream disturbances, measurements were performed with the sensors displaced in the streamwise as well as in the spanwise direction (to avoid interference). The resulting phase function is shown in figure 15 for two different values of the streamwise sensor spacing and two values of the unit Reynolds number (corresponding to $P_0 \sim 4.0$ and ~ 5.0 p.s.i.a.). The results confirm that the phase distribution does not depend significantly on the stagnation pressure (for measurements sufficiently close to the leading edge). An examination of figure 15 again reveals the occurrence of two relatively well-defined ranges of frequencies ($f < 5$ kHz and $9 < f < 25$ kHz) where, in this case, the phase function shows a linear behaviour in each region.

If we express the phase difference between the two signals as

$$\phi = \omega t_0,$$

where ω is the circular frequency and $t_0 = \Delta x/c_x$ (Δx is the sensor spacing in the x-coordinate and c_x is the streamwise propagation speed), then

$$\phi = 2\pi f \frac{\Delta x}{c_x}. \tag{5.5}$$

Thus, if from experiment we find that the phase depends linearly on the frequency, it implies that the streamwise disturbance velocity c_x is frequency independent. Furthermore, the above relation predicts that the slope $\mathrm{d}\phi/\mathrm{d}f$ will be dependent on Δx as is confirmed by the results in figure 15.

The results shown in figure 15 along with equation (5.5) were utilized to determine c_x. Linear fits in the 0–5 kHz large-wavelength high-coherence frequency range yielded an average of $c_x = 1286(\pm 7\%)\,\text{ft s}^{-1}$. The fact that $c_x/U \approx 0.64$ implies that

the acoustic wave fronts are propagating upstream with respect to the flow. Correspondingly $(U - c_x)/a = 1.07$ which also implies that the acoustic wave fronts are, on average, oblique to the x-axis.

We note that, in general, equation (5.5) can be applied only when the phase difference is measured with sensors solely displaced in x ($\Delta z = 0$). Since, in the experiments, a displacement in z was necessary to avoid wake interference from the upstream probe on the downstream sensor, we use the model to examine the applicability of equation (5.5) for the results of the present measurements. In the model with the four-component acoustic field, with $\Delta x \neq 0$ and $\Delta z \neq 0$, the cross-correlation between the sensors is

$$C(\tau) = \sum_i C_i(\tau) = \sum_i \frac{1}{T} \int_0^T h_i(x, y, z, t)\, h_i(x + \Delta x, y, z + \Delta z, t + \tau)\, \mathrm{d}t.$$

Introducing the expressions for h_i from equation (5.3) and performing the calculations gives

$$C(\tau) = 2A^2 \cos(k_z \Delta z) \cos(\omega\tau - k_x \Delta x). \tag{5.6}$$

Evidently, the spanwise displacement Δz appears only in the amplitude modulation term $\cos(k_z \Delta z)$ and the phase term is $2\pi f \Delta x / c_x$ as in equation (5.5). Note that, as in the case where Δx is zero, the phase will change by π when $k_z \Delta z = \pi/2$. This result follows from the assumption that the four waves in the model contribute equally to the correlation. For waves for which the wavelength is not large compared to the sensor spacing (as is the case for high-frequency components), we might expect a larger contribution to the correlation from waves with phase fronts approximately aligned with the straight line between the two sensors than from their symmetrical counterpart with opposite k_z. The unequally weighted contribution of high-frequency components to the correlation would result in a dependence on Δz of the phase term in equation (5.6). This may account for the phase change (in the frequency range $5 < f < 9\,\mathrm{kHz}$) being less than π for the higher value of Δx and the slight departure from linear behaviour observed above the phase jump ($f > 9\,\mathrm{kHz}$) for the results of the measurements reported in figure 15.

From the standpoint of the receptivity of the flat-plate boundary layer to the measured free-stream disturbance field, it is important to note that the measured value of $c_x/U \approx 0.64$ is close to the streamwise phase speed of the first mode instabilities for the zero-pressure-gradient boundary layer. Table 2 reports the values of the inferred streamwise wavelengths in the free stream ($\lambda_x = c_x/f$) for a number of disturbance frequencies of interest and the corresponding calculated streamwise wavelengths for the most unstable linear first mode waves (P. Balakumar 1998, private communication). The similarity in streamwise wavelengths between the measured free-stream acoustic disturbances and boundary layer instability waves is remarkable. Such a similarity is expected to promote the conversion from forced acoustic boundary layer oscillations to eigenmodes and possibly extend the region of receptivity to free-stream disturbances downstream of the leading-edge region. By contrast, at subsonic speeds the wavelength of free-stream sound waves is much larger than the streamwise wavelength of any unstable Tollmien–Schlichting waves at the same frequency. In this case, forced waves entering the boundary layer at the leading edge must experience a considerable reduction in wavelength as they progress downstream in order to match the spatial scale of the unstable boundary layer eigensolutions (Goldstein 1983; Lam & Rott 1960). It is also generally found that, because of the mismatch in wavelengths,

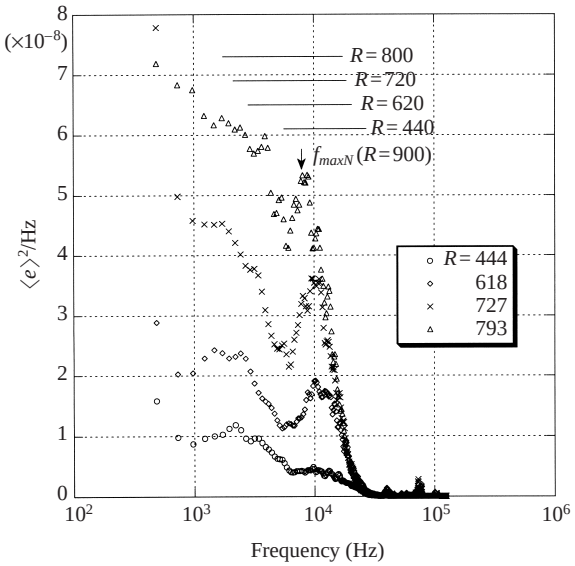

FIGURE 16. Spectra of the boundary layer fluctuations measured at several x-locations along the centreline of the flat plate. $Re/\text{in.} = 5.51 \times 10^4$. Solid lines indicate ranges of unstable frequencies (parallel linear stability theory, adiabatic wall – Balakumar).

the growth rate of the unstable modes in low-Mach-number boundary layers is not affected by acoustic free-stream disturbances.

6. Development of boundary layer disturbances and receptivity results at $P_0 = 4.0$ p.s.i.a.

The downstream development of the natural disturbances in the laminar boundary layer was investigated by measuring the fluctuations with hot wires at a number of x-locations on the plate. The hot-wire results reported in this section were collected utilizing the same hot wire at a fixed overheat ratio. Very small inconsequential drifts in wire properties (e.g. less than 1% change in wire resistance and cutoff frequency) were found throughout the investigation. Also, the total temperature variation between different experiments was found not to exceed 3 °K with a corresponding variation in hot-wire sensitivity of the order of 2% at $\eta \sim 6.0$.

6.1. *Frequency content of boundary layer oscillations*

The spectra of the voltage fluctuations measured in the boundary layer at several x-stations along the plate are shown in figure 16. The y-location of the measurements corresponds approximately to the inner peak of the double-hump broad-band distribution of the r.m.s. voltage fluctuation across the boundary layer ($\eta \sim 6.0$, § 4.2). Also indicated in figure 16 are the ranges of first-mode unstable frequencies as predicted by parallel linear stability theory for adiabatic wall conditions (P. Balakumar 1998, private communication) and the frequency of the maximum N factor (amplitude ratio) at $R = 900$ (L. M. Mack 1996, private communication). Note that the predicted unstable frequency range for $T_w = 1.1 T_{aw}$ is less than 10% larger than the unstable range corresponding to adiabatic wall conditions for the range of Reynolds number R of the measurements.

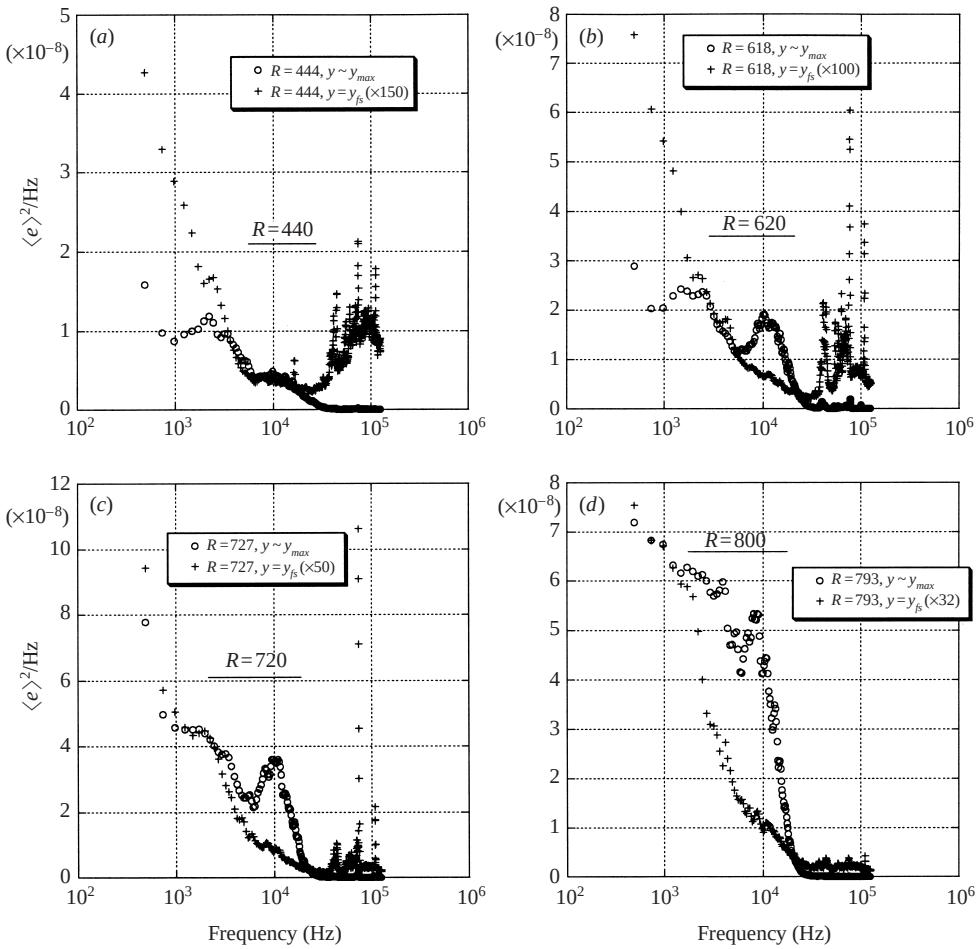

FIGURE 17. Spectra of the boundary layer and free-stream fluctuations measured at several x-locations along the centreline of the flat plate. $Re/\text{in.} = 5.51 \times 10^4$.

These results clearly show the energy growth, for a wide range of frequency components, as the Reynolds number R increases at the given free-stream unit Reynolds number. Noticeable is the increase in energy of disturbances at low frequencies outside the linear unstable range.

Figure 17 shows the same boundary layer spectra as in figure 16 together with the corresponding free-stream spectra. The free-stream frequency spectra have been scaled up by a variable factor (which depends on R) in order to match the lower frequency range of the boundary layer spectra where growth due to linear instability is not expected. The hump present in the free-stream spectra at $f \sim 80$–90 kHz is the result of electronic noise in the anemometry circuit, while the narrow spikes that occur at the high end of the spectrum are possibly due to mechanical vibrations of the wire and/or the probe–shaft assembly or strain-gauging effects.

At the first x-location corresponding to $R = 444$ (figure 17*a*), the shape of the spectrum in the boundary layer closely resembles the measured spectrum in the free stream above 2–3 kHz. It is not certain whether the difference at lower frequencies is due to experimental scatter or to a lower receptivity of the boundary layer with respect

to these very low frequencies. We discuss quantitative issues regarding receptivity and boundary layer disturbance growth in the next section but it can be qualitatively inferred from the spectra of the hot-wire voltage in figure 17 that acoustic forcing leads to a substantial amplification of free-stream disturbances in the boundary layer (note the scale factor of 150 in figure 17*a*), and also that low-frequency boundary layer disturbances, outside the unstable range, grow with distance downstream.

A particular feature revealed by the plots of the spectra measured in the boundary layer is the appearance of a relatively broad peak at $f \sim 10\,\mathrm{kHz}$ particularly evident downstream of the first x-station (figure 17*b*, *c*, *d*). The energy associated with this high-frequency band grows downstream and the corresponding peak becomes narrower as R increases. The high-frequency peak developing in the boundary layer fluctuation spectra has no counterpart in the free stream. In addition the high-frequency hump is contained in the linear unstable range and the corresponding frequency peak agrees very closely with the frequency of maximum N factor as predicted by linear theory (figure 16). The above remarks, together with the observation that the high-frequency peak shifts to lower frequencies as R is increased (at the given unit Reynolds number), demonstrate that this high-frequency development is directly linked to linear instability mechanisms.

No evidence of nonlinear wave evolution in the boundary layer, such as departure from similarity of the mean and fluctuation profiles and the emergence of high-frequency fluctuations (above the linear unstable range), was found at the low stagnation pressure of 4 p.s.i.a. for $x < 12\,\mathrm{in.}$

6.2. *Receptivity results and amplitude growth curves*

The narrow-band r.m.s. voltage (obtained from the spectrum) at the inner peak in the distribution across the boundary layer was determined at several x-stations from hot-wire surveys. Since the y-amplitude distributions show a satisfactory degree of similarity for $x < 12\,\mathrm{in.}$, the inner peak location of the r.m.s. voltage was found to correspond closely to a constant value of the similarity variable $\eta = 6.0\,(\pm 2\%)$ along the entire length under investigation. The only exception was found for measurements made close to the leading edge ($x \sim 3.5\,\mathrm{in.}$, $R \sim 440$) where, probably due to probe interference effects (see also § 3.1), the value of the similarity coordinate at the inner peak of the r.m.s. voltage distribution was found to be approximately 6% larger than further downstream. Fits to a large number of boundary layer calibration curves (a sample is shown in figure 5*a*), measured throughout the similarity region of the boundary layer flow, were differentiated to yield corresponding distributions of the hot-wire sensitivity. The average value of the sensitivity at $\eta = 6.0$ was then used to determine a representative r.m.s. mass-flux amplitude in the boundary layer $\langle \rho u \rangle_{BL}$. Notice that the value $\eta = 6.0$ corresponds to a location across the boundary layer which is below the location of the maximum r.m.s. mass-flux amplitude ($\eta_{max} = 7.2$, figure 6) and the amplitude at $\eta = 6.0$ is approximately 80% of the maximum amplitude. Also note that the value of the sensitivity at $\eta = 6.0$, determined from a boundary layer calibration, was found to be on average approximately 20% larger than the corresponding value determined from a free-stream calibration of the hot-wire (§ 4.2).

The growth of 1.4 kHz wide frequency band amplitudes for three selected frequency intervals has been examined. The non-dimensional values of the centre frequency are $F = 1.4 \times 10^{-5}$, $F = 5.0 \times 10^{-5}$, $F = 8.1 \times 10^{-5}$ and the corresponding values of the dimensional frequency for $Re/\mathrm{in.} = 5.51 \times 10^4$ are $f = 3\,\mathrm{kHz}$, $f = 10.5\,\mathrm{kHz}$ and $f = 17\,\mathrm{kHz}$ respectively.

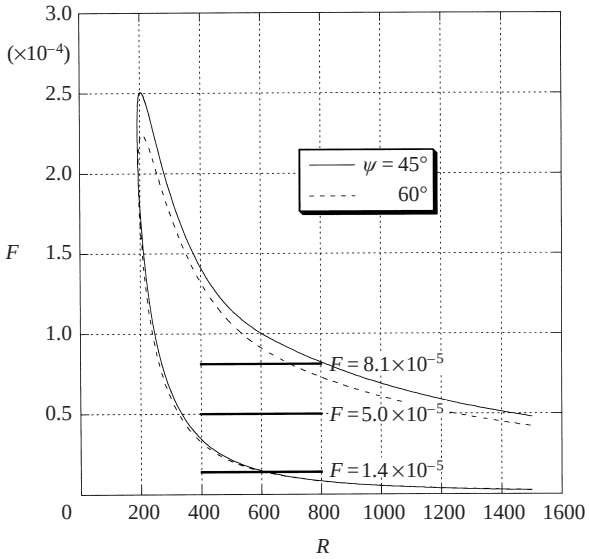

FIGURE 18. Neutral stability diagrams for two wave angles. $M = 2.98$, $T_0 = 278\,\mathrm{K}$ (parallel linear stability theory, adiabatic wall – Balakumar).

The intermediate frequency, $f = 10.5\,\mathrm{kHz}$, corresponds closely to the peak of the high-frequency hump in the spectrum in the explored range of Reynolds numbers (figure 16). According to the linear predictions, the low-frequency narrow band centred around $f = 3\,\mathrm{kHz}$ is expected to decay initially; this particular frequency was chosen so that the effect of acoustic free-stream forcing on the laminar boundary layer could be investigated since the corresponding frequency component in the free stream is relatively energetic. The highest frequency, $f = 17\,\mathrm{kHz}$, corresponds approximately to the upper limit of the unstable linear range where a sufficient amount of disturbance energy can still be measured at $P_0 \sim 4.0$ p.s.i.a. The neutral stability diagram computed by P. Balakumar (1998, private communication) for a Mach 2.98 laminar boundary layer is shown in figure 18 (parallel linear stability theory, adiabatic wall conditions). The measurement range of Reynolds number R for the selected frequency bands is also shown.

Before discussing the streamwise amplification of each of the narrow frequency bands, it is instructive to investigate quantitative receptivity issues concerning the excitation of boundary layer waves by free-stream disturbances in the leading-edge region. Figure 19(*a*) shows the free-stream amplitude level of two narrow frequency bands centred at $f = 3\,\mathrm{kHz}$ and $f = 10.5\,\mathrm{kHz}$ respectively, and corrected for the electronic noise, as a function of the unit Reynolds number (the highest frequency band at 17 kHz was not included because of the very low absolute level of the free-stream fluctuations and corresponding low signal-to-noise ratio at this frequency). The locations of the measurements in figure 19 are in the range $3.6 < x < 3.9$ in. The reasons why the free-stream disturbance level is seen to increase with unit Reynolds number are discussed in § 5.1. Figure 19(*b*) reports the ratio between the narrow-band r.m.s. mass-flux fluctuations measured at $\eta = 6.0$ and the corresponding free-stream value from figure 19(*a*). Ratios of 6 for the lower frequency and 10 for the higher frequency are obtained which, consistent with the observations made at the end of § 5.2, testify to the strong effect of acoustic free-stream forcing on the initiation of boundary layer waves. It is interesting to note that the ratio plotted in figure 19(*b*)

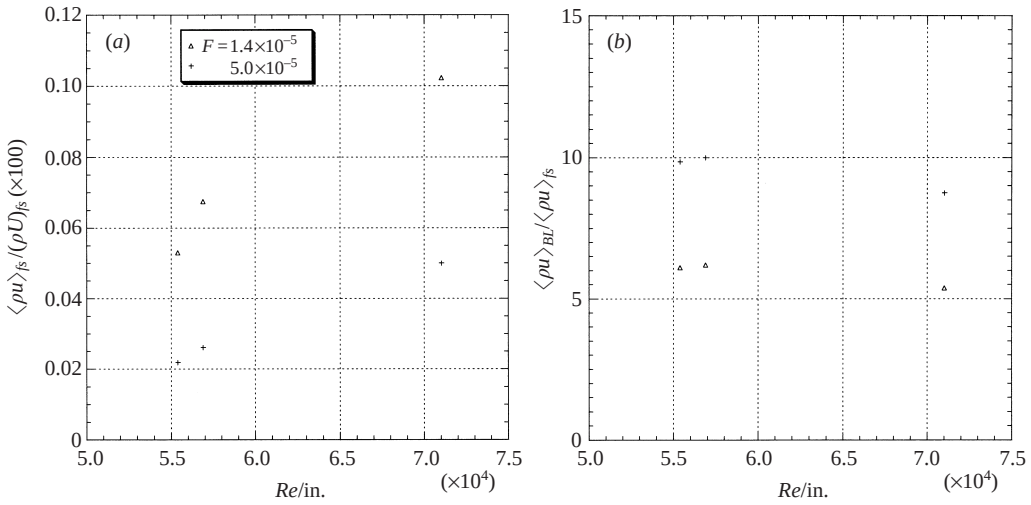

FIGURE 19. (*a*) Free-stream r.m.s. mass-flux amplitudes, (*b*) boundary layer r.m.s. mass-flux amplitudes normalized by the corresponding free-stream values. $x = 3.6$–3.9 in.

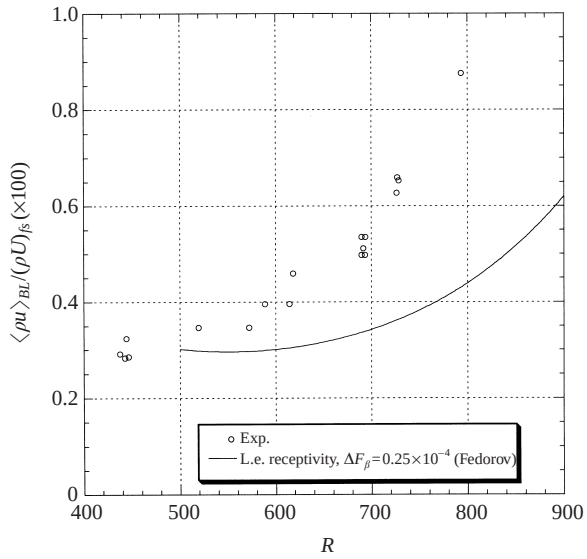

FIGURE 20. Growth curves of the boundary layer r.m.s. mass-flux amplitudes. Measurements vs. theoretical predictions (Fedorov). $F = 1.4 \times 10^5$, $Re/\text{in.} = 5.51 \times 10^4$.

appears to be relatively independent of the stagnation pressure: higher free-stream forcing initiates larger boundary layer waves in almost direct proportion. Finally, note that boundary layer modes are damped at the location of the measurements for $F = 1.4 \times 10^{-5}$ ($R_{cr} \sim 550$, $T_w = 1.1\ T_{aw}$) and instability growth begins upstream of the location of the measurements for $F = 5.0 \times 10^{-5}$ ($R_{cr} \sim 270$, $T_w = 1.1\ T_{aw}$) ($R = 444$ for the measurements at $Re/\text{in.} = 5.54 \times 10^4$ and $R = 527$ for the measurements at $Re/\text{in.} = 7.10 \times 10^4$ of figure 19).

The amplitude growth curves for the narrow frequency bands measured at $P_0 \sim 4.0$ p.s.i.a. are shown in figures 20–22. The continuous curves in these figures are the

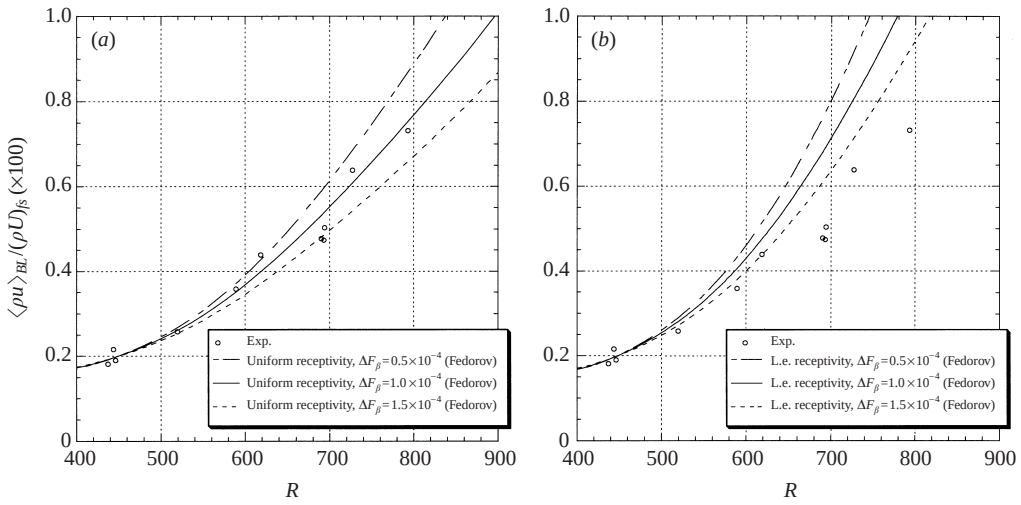

FIGURE 21. Growth curves of the boundary layer r.m.s. mass-flux amplitudes. Measurements vs. theoretical predictions (Fedorov): (*a*) uniform receptivity, (*b*) leading-edge receptivity. $F = 5.0 \times 10^5$, $Re/\text{in.} = 5.51 \times 10^4$.

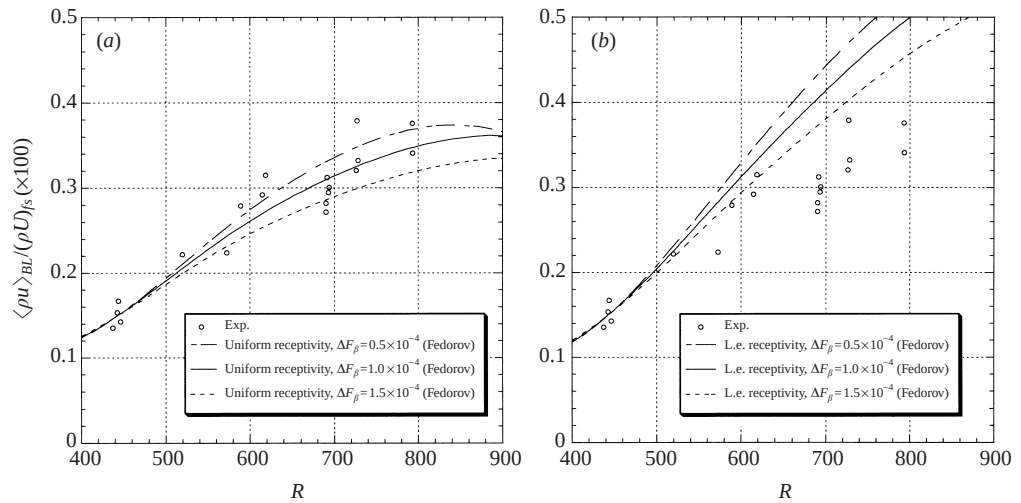

FIGURE 22. Growth curves of the boundary layer r.m.s. mass-flux amplitudes. Measurements vs. theoretical predictions (Fedorov): (*a*) uniform receptivity, (*b*) leading-edge receptivity. $F = 8.1 \times 10^5$, $Re/\text{in.} = 5.51 \times 10^4$.

results of calculations made by A. V. Fedorov (2002, private communication) and are based on a non-parallel linear stability theory ($M = 2.98$, $T_w = 1.1 T_{aw}$). Mode averaging, at a given frequency, has been performed to account for the contribution to the amplitude from a broad band of spanwise modes. In the experiment, a broad band of spanwise modes is expected to contribute to the amplitude of the boundary layer waves due to boundary layer receptivity to the three-dimensional free-stream acoustic field resulting from corner flow radiation. Since the spanwise spectrum of the boundary layer waves was not measured, calculations were performed for several values of the spanwise interval of integration ΔF_β ($F_\beta = \beta\nu/U$ is the non-dimensional

spanwise wavenumber and ΔF_β is such that $F_{\beta,max}$, $F_{\beta,min} = F_{\beta,m} \pm \Delta F_\beta$, where $F_{\beta,m}$ corresponds to the spanwise mode of maximum amplification). The effect of ΔF_β on the predicted amplitudes is shown in figures 21 and 22 respectively for $F = 5.0 \times 10^{-5}$ and $F = 8.1 \times 10^{-5}$. Evidently, the growth rate decreases as ΔF_β increases due to wave cancellation effects. This trend, however, is relatively weak. Note that $\Delta F_\beta = 1.0 \times 10^{-4}$ and $\Delta F_\beta = 1.5 \times 10^{-4}$ correspond respectively to approximately 2/3 of the unstable spanwise range and to the whole unstable spanwise range for $F = 5.0 \times 10^{-5}$ at $R = 800$ (A. V. Fedorov 2001, private communication). Finally, two simple receptivity assumptions, leading-edge receptivity and uniform distributed receptivity, were used to evaluate a receptivity density function included in the expression for the boundary layer disturbance amplitude (expression (A2) in the Appendix). Additional details regarding these predictions are provided in the Appendix.

Based on the data available from several runs, the maximum scatter affecting the measured amplitudes within the boundary layer appears to be of the order of 15–17%. Slight variations of stagnation pressure between runs, which affect the amplitude of the free-stream disturbances and consequently the induced boundary layer fluctuations, contribute to the dispersion in the data. The fitting procedure, which was used to determine the amplitude at $\eta = 6.0$ in the boundary layer, is an additional source of error in the experimental data. Finally, an uncertainty of approximately $\pm 10\%$ was found when determining the average value of the sensitivity at $\eta = 6.0$. The uncertainty in the sensitivity affects the absolute value of the r.m.s. mass-flux fluctuations but it does not affect the growth rates, as inferred from figures 20–22.

Figure 21 illustrates the streamwise amplitude growth of the 10.5 kHz narrow band. In this case, the investigated range of the Reynolds number lies entirely in the region of instability for this frequency component. In figures 21 and 22, the calculated amplitudes are scaled to match the corresponding experimental values at $R = 440$. Indeed, the calculations yield the disturbance amplitudes up to an arbitrary constant since no attempt was made to evaluate quantitatively the receptivity density function on the basis of the available measurements in the free stream (see the Appendix).

The agreement between measured and calculated growth rates is good in the case where a uniform receptivity assumption is used for the calculations (figure 21*a*). With a leading-edge receptivity assumption, the theoretical model tends to overpredict the observed experimental amplitude growth (figure 21*b*). These results support a hypothesis that, due to the observed streamwise wavelength matching between free-stream disturbances and boundary layer eigenmodes (§ 5.2), receptivity to free-stream disturbances is not confined to the leading edge, as is the case for incompressible boundary layer flow, but it extends downstream of the neutral branch through the region of unstable mode development. Despite the larger experimental scatter in the data, due to the small disturbance amplitudes at high frequencies (and therefore larger noise-to-signal ratio), similar good agreement between measurements and calculations is shown in figure 22(*a*) for the streamwise growth at the highest frequency of $f = 17$ kHz. Further calculations (not reported) show that these growth rates are underpredicted by approximately 20% if a parallel assumption for the mean boundary layer flow is used in the theoretical model.

We conclude that, for these frequency components (for which the corresponding free-stream spectral energy is very small, figure 13), eigenmode instability and uniform distributed receptivity are the dominant mechanisms in determining the growth rate downstream of the neutral branch of the stability diagram.

The behaviour of the 3 kHz frequency component is displayed in figure 20. Note that in figure 20, the theoretical amplitudes have been scaled so that at the neutral point ($R_{cr} = 550$) they match the experimental amplitude at $R = 440$. Evidently, the experimental measurements indicate an early amplitude growth which is not consistent with the results of the linear stability analysis. In addition the experimental growth rate in the theoretical unstable region ($R > R_{cr}$) is substantially higher than the predicted one despite the low value of $\Delta F_\beta = 0.25 \times 10^{-4}$ selected for the calculations of the amplitude of the 3 kHz component.

The anomalous growth of low-frequency components may be explained in terms of forcing mechanisms whereby acoustic boundary layer disturbances, resulting from the direct interaction of free-stream acoustic waves with the boundary layer, grow downstream starting from the leading-edge region. According to a forcing theory (Mack 1975), the ratio between the maximum amplitude across the boundary layer and the free-stream amplitude of an acoustic disturbance grows to a maximum at a distance downstream of the leading edge whose value is inversely proportional to the frequency. In addition, the magnitude of this maximum is inversely proportional to the frequency (Mack 1975). These results are found to be valid regardless of the disturbance wave angle and wave velocity (as long as the latter, c_x, is supersonic relative to the free-stream velocity) (Mack 1975).

Mack finds a ratio of the maximum amplitude of the forced response in the boundary layer to the amplitude in the free stream of approximately 7 at Mach 3, $R = 440$ and $T_w = 0.8 T_{aw}$ for an oblique acoustic wave (wave angle equal to 55°) of non-dimensional frequency $F = 1.5 \times 10^{-5}$ propagating with a speed equal to 0.4 times the free-stream velocity (Mack 1975). In spite of differences between some of the parameters for this prediction and those for the present experiments (in particular the propagation speed of the disturbances, the temperature at the plate surface and the fact that, in the experiments, a broad band of spanwise components are expected to contribute to the measured disturbance), the predicted value of the amplitude ratio compares well with the corresponding value of approximately 7.5 (the ratio of 6 from figure 19(*b*) is measured at $\eta = 6.0$ where the amplitude is 80% of the maximum value) measured at $R = 444$ ($Re/\text{in.} = 5.54 \times 10^4$) for the same disturbance frequency ($F = 1.5 \times 10^{-5}$). Mack (1975) finds that the propagation speed of the disturbances has little effect on the forced boundary layer response and also that the wall temperature has almost no influence on the forced response for $0.8 < T_w/T_{aw} < 1$ and for a wave angle of 55°.

These theoretical findings and the fact that, for the present experiment, most of the free-stream energy is concentrated at low frequencies ($f < 5$ kHz) may explain the disagreement between the measurements and the results of the stability calculations in the case of the 3 kHz frequency component. Note, however, that the forcing theory of Mack predicts a decrease of the amplitude of these forced acoustic disturbances downstream of the neutral branch. Thus, the anomalous growth rate of the 3 kHz narrow frequency band for $R > R_{cr}$ could be the result of the growing free-stream disturbances, with distance downstream, in the experiment (the amplitude of the incoming free-stream wave is assumed to be uniform in the forcing theory of Mack 1975).

Additional measurements, conducted at a slightly higher value of $Re/\text{in.} = 5.74 \times 10^4$ ($P_0 \sim 4.2$ p.s.i.a.), indicate that a slight change in unit Reynolds number produces an overall upward shift in the absolute values of the amplitudes (due to the corresponding increase in free-stream disturbances), but it does not affect the growth rates which are found (Graziosi 1999).

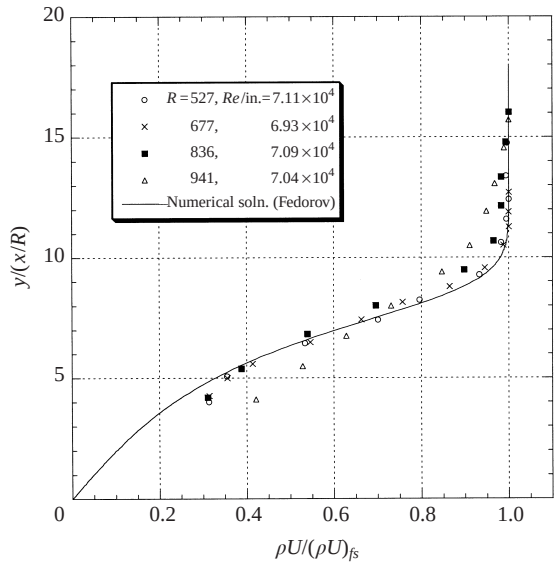

FIGURE 23. Mean boundary layer profiles at $P_0 \sim 5.0$ p.s.i.a. Hot-wire measurements and boundary layer calculations.

7. The development of transition at $P_0 = 5.0$ p.s.i.a.

Figure 23 shows the mean boundary layer profiles measured at several streamwise stations along the plate at $P_0 \sim 5.0$ p.s.i.a. The data were collected using a hot-wire sensor calibrated in the free stream. As discussed in § 4.2, the free-stream calibration procedure does not yield reliable distributions of the mass-flux sensitivity across the boundary layer but, in general, the resulting laminar mean profile shows a satisfactory agreement, above the sonic line, with the Pitot-static measurements and the boundary layer calculations. The first significant departure from similarity is observed to occur at $x \sim 9$–10 in. (profile at $R = 836$ in figure 23). The results show that the outer part of the layer deviates from the laminar profile first and, as the Reynolds number increases further, progress towards a fuller profile is found (see also figure 3).

Examination of the frequency content of the fluctuations (figure 24), measured at a distance from the plate surface corresponding to the position of the maximum broad-band r.m.s. voltage, shows the rapid development of low-frequency components in a region of the flow where the mean profile departs from similarity ($R = 836$ and $R = 941$). (It was found that the high-frequency spikes in these spectra were the result of mechanical vibrations of the sensor and/or strain-gauging effects.) Figure 25 presents a magnification of the high end of the frequency spectrum at $P_0 \sim 4.0$ p.s.i.a. (figure 25*a*) and $P_0 \sim 5.0$ p.s.i.a. (figure 25*b*). At the lower stagnation pressure, high-frequency components, which lie outside the unstable linear range, decay as the Reynolds number R increases in a manner which is consistent with linear stability theory. Conversely, at the higher unit Reynolds number conditions (figure 25*b*), very high frequencies ($f > 30$ kHz) are observed to grow considerably throughout the whole range of R examined.

7.1. *Growth curves and boundary layer amplitude distributions*

The broad-band mass-flux amplitudes, measured at $P_0 \sim 5.0$ and ~ 4.0 p.s.i.a. and at a location corresponding to the maximum value of the broad-band r.m.s. voltage

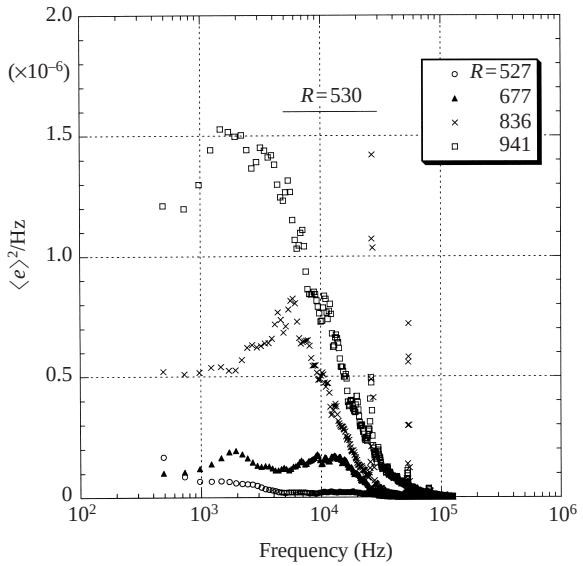

FIGURE 24. Spectra of the boundary layer fluctuations measured at several x-locations along the plate centreline. Solid line indicates range of unstable waves at $R = 530$ (parallel linear stability theory, adiabatic wall – Balakumar). $Re/\text{in.} = 7.04 \times 10^4$.

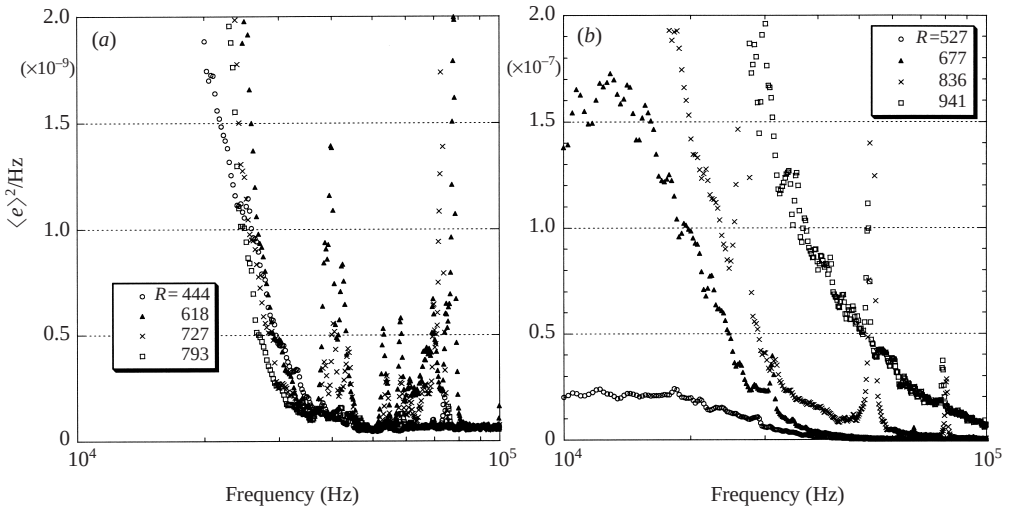

FIGURE 25. Magnification of the high-frequency range in the spectra of the boundary layer fluctuations. (*a*) $P_0 \sim 4.0$ p.s.i.a., (*b*) $P_0 \sim 5.0$ p.s.i.a.

distribution across the boundary layer, are shown in figure 26. Amplitudes determined both with a boundary layer calibration and a free-stream calibration of the hot wire (§4.2) are included in the figure. Amplitudes determined with a boundary layer calibration are not available for $P_0 \sim 5.0$ p.s.i.a. at the two most downstream measurement locations ($R > 800$) because of the departure from similarity of the mean profile and the lack of detailed Pitot-static measurements in the transition region. Note that, in the similarity region, the mass-flux amplitudes, determined from a free-stream calibration, appear to be overpredicted by a maximum of approximately

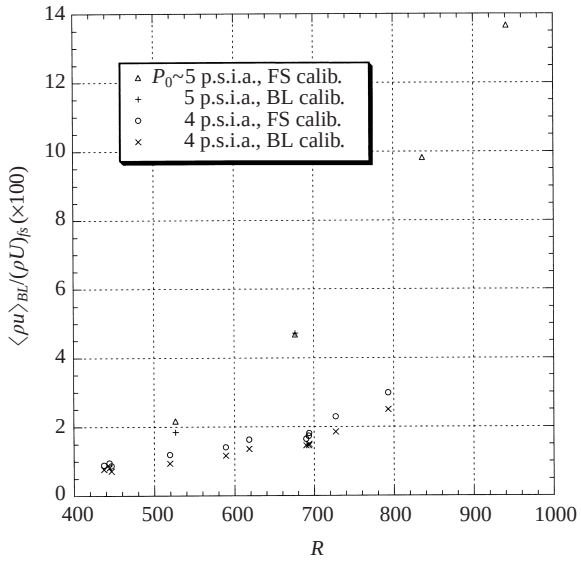

FIGURE 26. Growth curves of broad-band r.m.s. mass-flux amplitudes in the boundary layer.

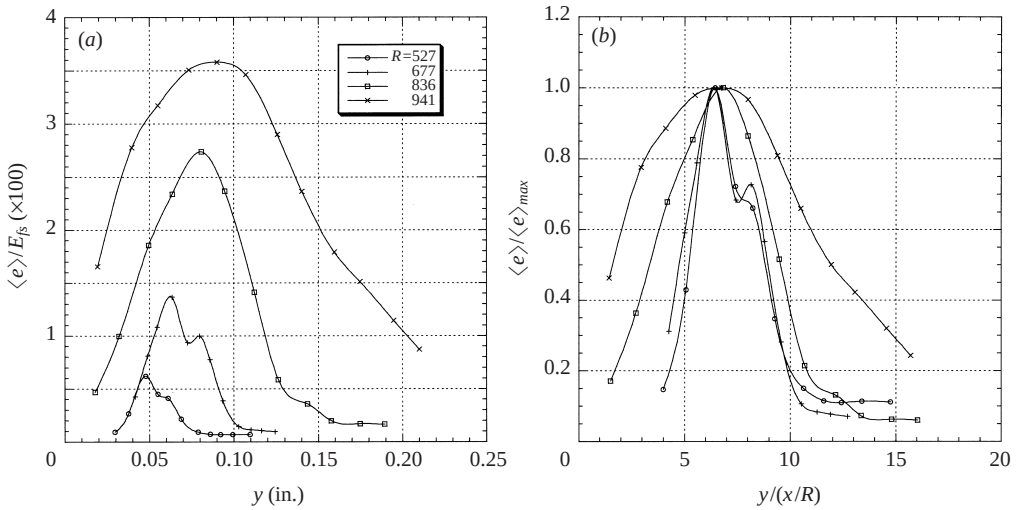

FIGURE 27. Broad-band r.m.s. voltage distributions across the boundary layer measured at a number of x-stations along the plate centreline: (a) physical coordinates, (b) similarity coordinates. $Re/\text{in.} = 7.04 \times 10^4$.

25% with respect to the amplitudes determined from a boundary layer calibration. At the location where the mean boundary layer profile is first observed to depart from the similarity solution ($R \sim 800$, $P_0 \sim 5.0$ p.s.i.a.), the broad-band amplitude in figure 26 is approximately 10% of the free-stream mean mass flux.

Broad-band r.m.s. voltage distributions across the boundary layer are presented in figure 27. The profiles measured at $R = 527$ and $R = 677$ collapse reasonably well in similarity coordinates (figure 27b) and, as for corresponding measurements at $P_0 \sim 4.0$ p.s.i.a., they are characterized by a double-hump shape. Profiles corresponding to selected narrow frequency bands display the same qualitative behaviour as the

broad-band amplitude profiles (Graziosi 1999). A departure of the fluctuation profiles from similarity takes place further downstream at a distance which corresponds to a location where the mean profile departs from similarity ($R = 836$; figure 27*b*). The main feature of the y-distributions of the r.m.s. voltage measured at later stages of transition ($R = 836$ and $R = 941$; figure 27*b*) is a relatively higher growth rate of the fluctuations in the wall and outer region of the boundary layer with respect to the region of the peak which gives rise to fuller profile shapes as R is increased. Analysis of the time traces of the oscillating voltage show that this change is linked to the appearance of energetic spike-like structures in the wall and outer flow regions of the boundary layer.

7.2. *An analysis of the time traces of the fluctuating voltage at transition*

To help reveal the character of the nonlinearities which develop as the transition region is approached, the time histories of the fluctuating voltage were examined.

Figures 28–31 show time traces measured at four streamwise stations at several locations across the boundary layer (δ_{lam}, in the figures, is the thickness of a laminar boundary layer at the corresponding R). At the most upstream station ($R = 527$, figure 28) quasi-periodic waves ($f = 10$–30 kHz) are apparent in the time trace collected in the region where the peak in the broad-band amplitude distribution occurs (figure 28*b*). The signal clearly appears to be composed of high-frequency components residing in the linearly unstable portion of the spectrum and low frequencies (e.g. 2 kHz) which have been previously linked to amplification of forced acoustic disturbances.

Evidence of strong nonlinear development appears downstream at $R = 677$ (figure 29). Correspondingly, the broad-band mass-flux amplitude in figure 26 reaches a value of 4.5–5%. Single spike-like features occur close to the plate surface and in the outer portion of the boundary layer (figures 29*a* and 29*c*) whereas short large-amplitude oscillations at the frequency of the instability waves emerge occasionally in the hot-wire waveform at $y/\delta_{lam} \sim 0.7$ (figure 29*b*). It is interesting to note that the spikes point upward in the wall region (higher than average mass flow rate) and downward in the outer part of the layer (lower than average mass flow rate) directly contributing to mixing enhancement throughout the boundary layer. It is important to emphasize that the spikes in the boundary layer are the result of mechanisms inherent to the flat-plate boundary layer transition process and are not a consequence of direct forcing from free-stream disturbances. Figures 29(*d*)–29(*g*) show the time traces of the free-stream fluctuating voltage at different heights above the plate (note the change of the time scale between figures 29(*a–c*) and 29(*d–g*)). The intensity of the spikes diminishes as y/δ_{lam} increases. Eventually, for $y/\delta_{lam} \geqslant 1.27$, no recognizable large events appear in the time traces of the hot-wire fluctuating voltage. It is also important to note that at this stage of the transition process, the mean boundary layer profile and the y-distributions of the r.m.s. voltage have not yet departed from similarity: the occurrence of the spikes in the time signals is not yet statistically sufficiently significant to affect the average measurements. An early additional indication of nonlinearity, however, is the observed growth of very high-frequency components in the spectrum as discussed at the beginning of this section (figure 25*b*). While no correlation measurements were made, it is interesting to notice that the time scales between spikes in figure 29 appear to be qualitatively consistent with the time scales of low-frequency fluctuations which have been linked to amplification of forced acoustic disturbances. This observation suggests that forced acoustic boundary layer

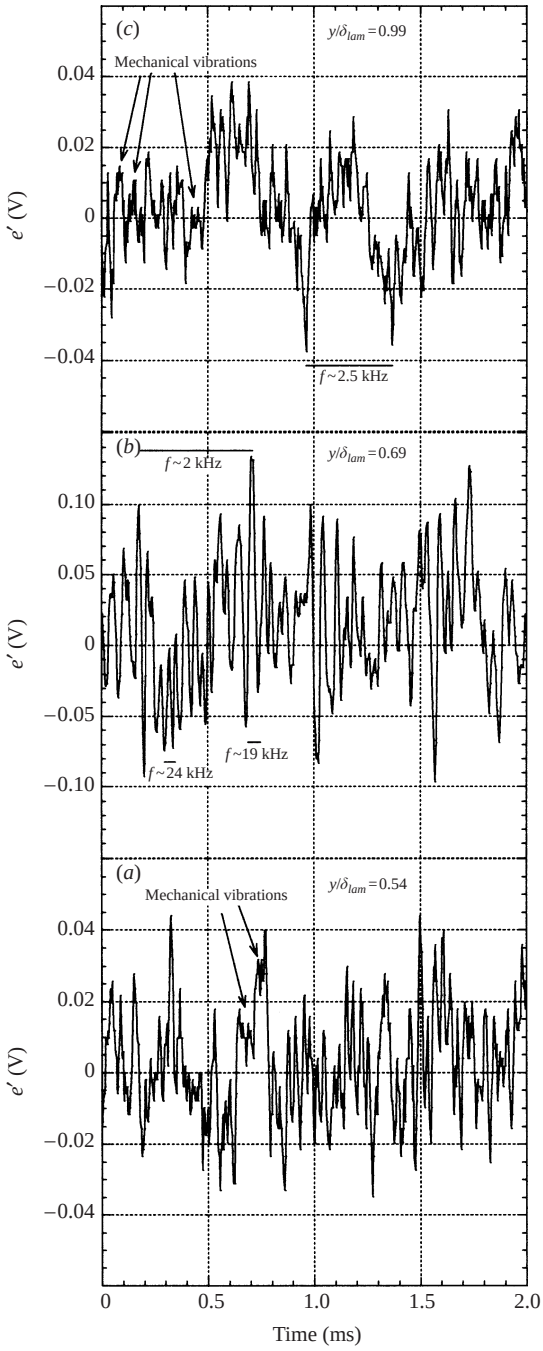

FIGURE 28. Time traces of the fluctuating hot-wire voltage. $R = 527$, $Re/\text{in.} = 7.04 \times 10^4$.

disturbances may play an active role in the transition process and directly contribute to the development of nonlinearities.

The first departure of the mean and r.m.s. profiles from similarity occurs at a downstream station corresponding to $R \sim 800$ and the time histories of the fluctuating voltage are presented in figure 30 at five different heights in the boundary

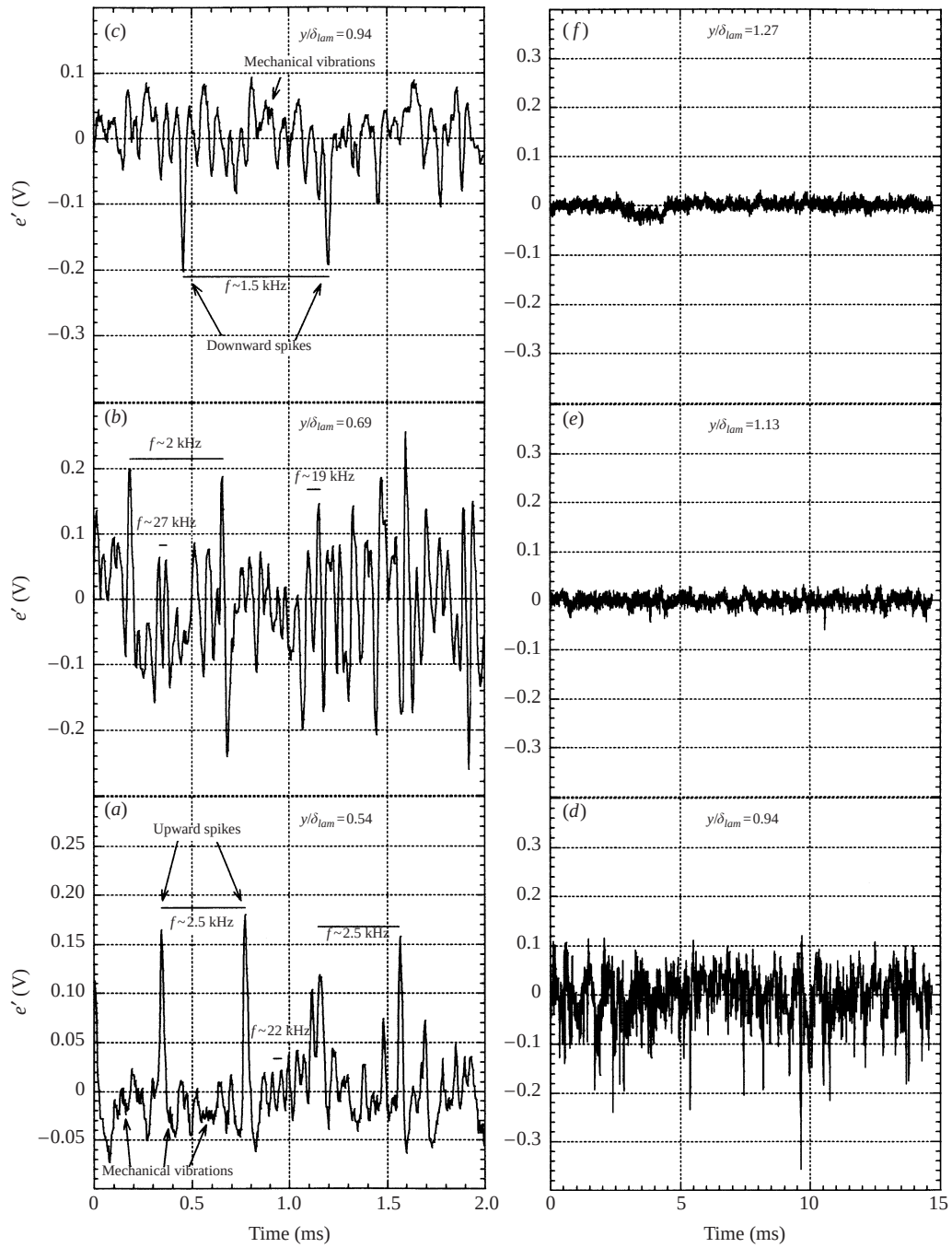

FIGURE 29(*a–f*). For caption see next page.

layer for $R = 809$. The evolution of the spike-like events, above and below the location of maximum amplitude, continues and the occurrence of the spikes is now more frequent. Close to the wall, traces with double upward spike-like structures appear (figure 30*a*, *b*). Figure 30(*d*) shows that multiple spikes tend to emerge in the outer region as well. In addition, the extent of the inner and outer regions across

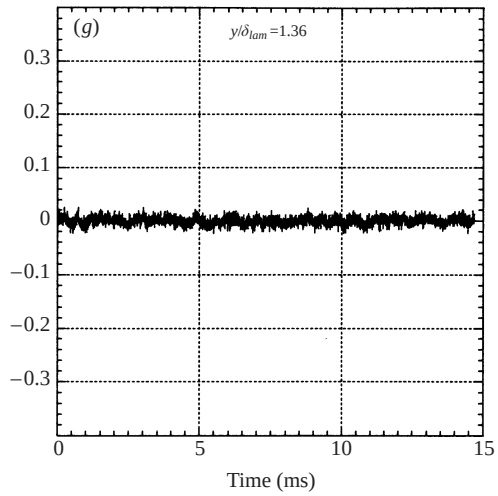

FIGURE 29. Time traces of the fluctuating hot-wire voltage. $R = 677$, $Re/\text{in.} = 7.04 \times 10^4$.

the boundary layer where the large events are measured grows considerably as the Reynolds number R increases. It is interesting to note that the region where the upward events take place develops approximately around the location of maximum Reynolds stress due to linear instability waves ($y/\delta_{lam} \sim 0.5$; L. M. Mack 1996, private communication).

The time traces lose any regular pattern and display a chaotic behaviour further downstream at $R = 941$ (figure 31). The fuller shape of the mean profile (figure 23) and the r.m.s. voltage distributions (figure 27) at the corresponding x-location clearly indicate that the transition process has reached a late stage. Close to the wall, multiple spikes coalesce (figure 31a, b). Large events are now noticeable everywhere across the boundary layer.

Kachanov and collaborators (see the review paper by Kachanov 1994) have studied in detail the mechanics of the formation and development of the spike occurring in the K-regime of transition for the incompressible boundary layer. In addition, Borodulin & Kachanov (1990) drew attention to upward 'saw-like' structures close to the wall which occurred at late stages of transition concurrently with the appearance of the downward spikes in the outer region of the Blasius boundary layer. Figure 30 in Kachanov (1994), shows oscilloscope traces measured in a transitional incompressible boundary layer at various distances from the wall. The qualitative resemblance with the time traces reported in figure 31 is clear (the high coherence of the structures in figure 30 in Kachanov 1994 is due to the artificial generation of the disturbances). As in the present experiment, the spikes in Kachanov's traces are found before any significant distortion of the mean profile takes place.

8. Conclusions

The paper has presented and discussed results concerning stability, receptivity and transition to turbulence in a Mach 3 flat-plate boundary layer for a slightly heated wall condition ($T_w = 1.1 T_{aw}$).

The wind tunnel was operated at low stagnation pressure conditions ($P_0 \sim$ 4–5 p.s.i.a.; $Re/\text{in.} \sim 5.5 \times 10^4$–$7.0 \times 10^4$) and the mass-flux free-stream disturbance level at the lowest unit Reynolds number ($Re/\text{in.} \sim 5.5 \times 10^4$) was found to be 0.11% with most of the energy concentrated at frequencies below the first-mode unstable

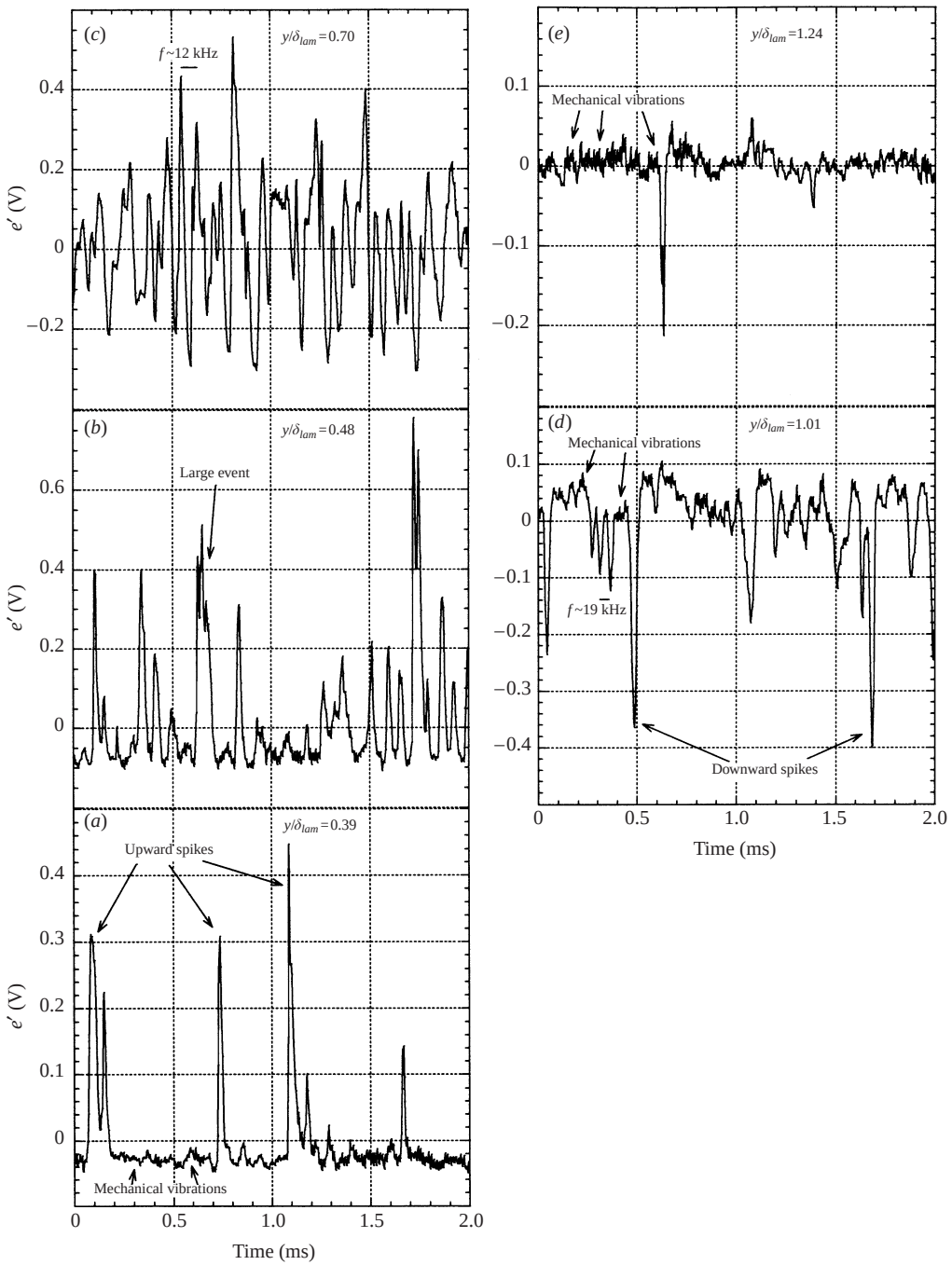

FIGURE 30. Time traces of the fluctuating hot-wire voltage. $R = 809$, $Re/\text{in.} = 7.04 \times 10^4$.

range ($f < 5\,\text{kHz}$). The nozzle-wall boundary layers were laminar at the lowest unit Reynolds number of the experiments, with the exception of residual disturbances measured in the nozzle corners.

An investigation of the disturbance environments in the free stream and on the nozzle walls was undertaken prior to exploring the flat-plate boundary layer flow.

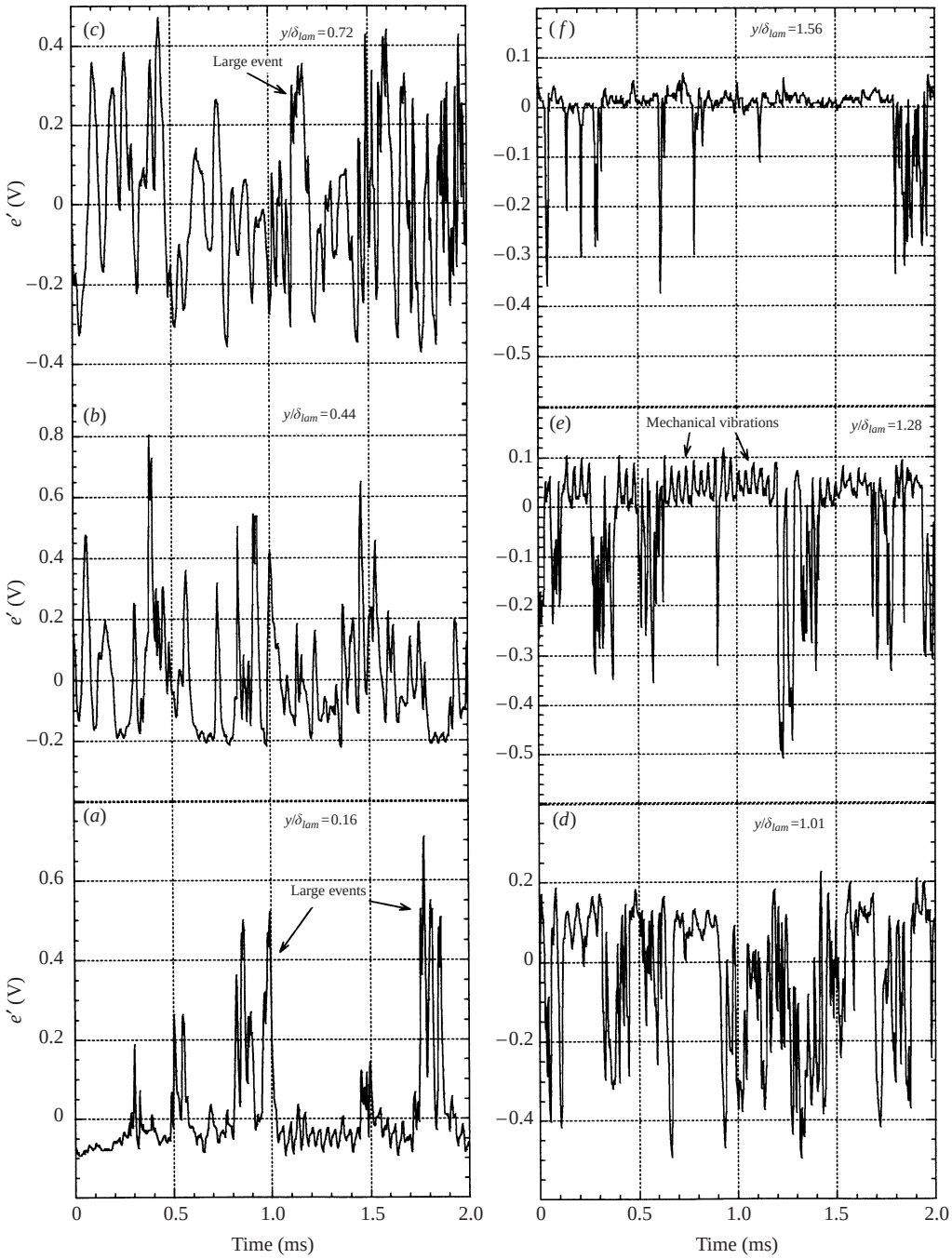

FIGURE 31. Time traces of the fluctuating hot-wire voltage. $R = 941$, $Re/\text{in.} = 7.04 \times 10^4$.

Notwithstanding the low disturbance level, a picture of a well-correlated acoustic disturbance field in the test section emerged from hot-wire and hot-film measurements and corresponding physical modelling. The measurements also showed that corner disturbances were the primary source of free-stream fluctuations at the low stagnation pressure of approximately 4 p.s.i.a. and as far as $x \sim 9$–10 in. downstream of the

leading edge along the plate centreline. The non-dimensional propagation speed of the free-stream disturbances was found to be approximately 0.64 (approximately independent of frequency), which was shown to yield streamwise wavelengths which are remarkably close to the wavelengths of the corresponding first-mode instability waves.

Amplitude distributions across the boundary layer were measured in detail. The r.m.s. voltage distributions and the r.m.s. mass-flux distributions obtained by calibrating the hot wire in the free stream displayed a double-peak shape, which has also been found by previous authors at Mach 3 (e.g. Kendall 1975). It was shown that, at least in the present case, this unexpected behaviour is not the result of a genuine flow phenomenon (as has been proposed) but rather a consequence of the change in the mass-flux sensitivity of the hot-wire sensor within the boundary layer, arguably due to Reynolds and Knudsen number effects. When the hot wire was calibrated against the mean boundary layer profile, a single-peak amplitude distribution was established which is consistent with the computed eigenfunction. This boundary layer calibration procedure was then used to determine streamwise distributions of the r.m.s. mass-flux disturbance amplitude for a number of frequency bands.

Measurements made in the leading-edge region ($3.6 < x < 3.9$ in.) show that the free-stream acoustic disturbances interact with the boundary layer and initiate mass-flux boundary layer oscillations which, at the location of the measurements, were found to be 6 times larger at $F = 1.4 \times 10^{-5}$ and 10 times larger at $F = 5.0 \times 10^{-5}$ than the corresponding disturbances in the free stream. Downstream from the leading edge, at the lowest unit Reynolds number of the investigation ($Re/\text{in.} \sim 5.5 \times 10^4$, $P_0 \sim 4.0$ p.s.i.a.), low-frequency boundary layer waves (e.g. $F = 1.4 \times 10^{-5}$) were observed to grow in a region both upstream and downstream of the neutral branch and in a manner which is inconsistent with theoretical results based on stability theory. The maximum boundary layer amplitude of a frequency component $F = 1.4 \times 10^{-5}$, relative to the free-stream amplitude and measured upstream of the neutral branch, is consistent with the results of the acoustic forcing theory of Mack (1975). On the other hand, good agreement between the measurements and the results of non-parallel linear stability theory showed that the growth of a well-defined unstable high-frequency band (peaked at $F \sim 5.0 \times 10^{-5}$), for which the corresponding free-stream disturbance energy is very small, is due to mechanisms of linear instability and distributed receptivity. Comparisons between measured and predicted growth rates for these high-frequency boundary layer waves provide evidence that the region of receptivity is not confined to the leading edge, as in the incompressible case, but extends downstream of the neutral branch through the region of instability growth (distributed receptivity). In the experiments, the close matching of streamwise wavelength between free-stream disturbances and eigenmodes adds support to this hypothesis. These results on receptivity are being followed by further study using direct acoustic forcing.

The late stages of transition were also investigated at a higher unit Reynolds number $Re/\text{in.} \sim 7.0 \times 10^4$ ($P_0 \sim 5.0$ p.s.i.a.) with a correspondingly higher free-stream turbulence level of 0.39%. High-frequency components (outside the linear unstable range) were found to grow throughout the range of Reynolds number R explored ($500 < R < 950$). This growth is most likely linked to the development of nonlinearities which give rise to spike-like structures in the time traces of the fluctuating voltage. Any possible connection between the spikes and low-frequency forced acoustic disturbances is a subject for further work. The distortion of the similarity shape of the mean boundary layer profile and of the disturbance amplitude

profile occurs downstream of the location where the spikes are first observed. The broad-band mass-flux amplitude, measured at a location across the boundary layer where the r.m.s. voltage fluctuation peaks, was found to be approximately 4.5–5% at the x-station where the spikes were first detected and approximately 10% at the x-station where departure from similarity of the mean and r.m.s. amplitude profiles was observed.

Qualitative comparisons with results reported by Kachanov (1994) in an incompressible two-dimensional boundary layer indicate a resemblance in the main features of the time traces for the late stages of transition.

The support by AFOSR under Grants F49620-93-1-0427 and F49620-99-1-0066 is gratefully acknowledged. The authors also wish to acknowledge the contribution to this work by A. V. Fedorov and the valuable comments and theoretical results provided by Drs P. Balakumar, J. M. Kendall and L. M. Mack.

Appendix

By A. V. Fedorov
Moscow Institute of Physics and Technology,
16 Gagarin Street, Zhukovski 140160, Russia

Under the assumption that a first-mode wave of eigenvalue $\alpha_{fm}(\beta,\omega)$ (where α,β and ω are the streamwise and spanwise wavenumbers and frequency respectively) is excited by a corresponding acoustic wave component (α_a,β,ω) of amplitude A_a, the amplitude of the former can be expressed as

$$A_{fm} = A_a C_{a\to fm}(x_0) q_{fm}(y_m,x) \exp\left(\int_{x_0}^{x} \mathrm{i}\alpha_{fm}(x)\,\mathrm{d}x + \mathrm{i}\beta z\right), \quad x > x_0, \tag{A 1}$$

where $C_{a\to fm}$ is a receptivity coefficient evaluated at the initial point x_0, and $q_{fm}(y_m,x)$ is the first-mode eigenfunction calculated at the point y_m of maximum mass-flux disturbance.

In the more general case where receptivity is distributed over an axial length $x_{00} \leqslant x_0 \leqslant x_{01}$ and several transverse modes contribute to the overall amplitude such that the β-spectrum is different from zero in a range $\beta_{min} \leqslant \beta \leqslant \beta_{max}$, the r.m.s. amplitude of a first-mode wave with frequency ω is derived from averaging expression (A 1) over β and x_0:

$$A^2_{fm,rms} = \frac{\text{const}}{x_{01}-x_{00}} \int_{x_{00}}^{x_{01}} \left[\frac{1}{\beta_{\max}-\beta_{\min}} \int_{\beta_{\min}}^{\beta_{\max}} |A_a G_{a\to fm}(x_0,\beta) q_{fm}|^2 \right.$$
$$\left. \times \exp\left(-2\int_{x_0}^{x} \alpha_{fm}\,\mathrm{d}x\right)\mathrm{d}\beta\right]\mathrm{d}x_0, \tag{A 2}$$

where $G_{a\to fm}(x_0,\beta)$ is a receptivity density function.

Expression (A 2) has been evaluated using a multiple scales method (Tumin & Fedorov 1982) for a number of frequencies ω and β-intervals of integration to predict the amplification of boundary layer fluctuations and to compare with the corresponding growth rates of the measured boundary layer disturbances (figures 20–22).

The shape of the receptivity density function $G_{a\to fm}(x_0,\beta)$ has been determined according to two different receptivity assumptions. For the case of 'leading-edge

receptivity', acoustic disturbances are assumed to be internalized by the laminar boundary layer in the leading-edge region, consequently the receptivity density function is chosen to be a delta function concentrated along the plane $x_0 = \text{const}$ (where x_0 is a streamwise distance from the geometrical leading edge of the order of the first-mode wavelength). The model assumes a uniform amplitude distribution as a function of β at x_0. For the 'uniform receptivity' hypothesis, the receptivity density function is assumed to be constant for $x > x_0$ over the entire surface of the plate (again, x_0 is a streamwise distance from the leading edge of the order of the first-mode wavelength). This second model simulates the case where acoustic receptivity occurs over the entire plate surface.

Finally, the theoretical eigenfunctions included in figures 4(b) and 6 were calculated as the r.m.s. values

$$\langle \rho u \rangle(\eta) = \sqrt{\frac{1}{\beta_{\max} - \beta_{\min}} \int_{\beta_{\min}}^{\beta_{\max}} q_{fm}^2(\eta)\, \mathrm{d}\beta}.$$

REFERENCES

Balachandar, S. & Malik, M. R. 1995 Inviscid instability of streamwise corner flow. *J. Fluid Mech.* **282**, 187–201.

Beckwith, I. E., Creel, Jr, T. R., Chen, F.-J. & Kendall, J. M. 1983 Free stream noise and transition measurements in a Mach 3.5 pilot quiet tunnel. *AIAA Paper* 83-0042.

Beckwith, I. E. & Miller III, C. G. 1990 Aerothermodynamics and transition in high-speed wind tunnels at NASA Langley. *Annu. Rev. Fluid Mech.* **22**, 419–439.

Borodulin, V. I. & Kachanov, Y. S. 1990 Experimental study of soliton-like coherent structures in boundary layer. *Proc. Scientific & Methodological Seminar on Ship Hydrodynamics*, 19th Session, vol. 2, pp. 99-1–99-10. Varna: Bulg. Ship Hydrodyn. Centre.

Brown, W. B. 1962 Exact numerical solutions of the complete linearized equations for the stability of compressible boundary layers. *Rep. NOR*-62-15, Northrop Aircraft Inc., CA.

Bushnell, D. M. 1990 Notes on the initial disturbance fields for the transition problem. In *Instability and Transition* (ed. M. Y. Hussaini & R. G. Voigt), vol. 1, pp. 217–232. Springer.

Chang, C.-L. & Malik, M. R. 1994 Oblique-mode breakdown and secondary instability in supersonic boundary layers. *J. Fluid Mech.* **273**, 323–360.

Chen, F. J., Malik, M. R. & Beckwith, I. E. 1989 Boundary layer transition on a cone and flat plate at Mach 3.5. *AIAA J.* **27**, 687–693.

Demetriades, A. 1989 Growth of disturbances in a laminar Boundary layer at Mach 3. *Phys. Fluids* A **1**, 312–317.

Dryden, H. L. 1955 Transition from laminar to turbulent flow at subsonic and supersonic speeds. *Proc. Conf. on High-Speed Aeronautics*, 41, Polytechnic Institute of Brooklyn.

El-Hady, N. M. 1992 Secondary instability of high speed flows and the influence of wall cooling and suction. *Phys. Fluids* A **4**, 727–743.

Erlebacher, G. & Hussaini, M. Y. 1990 Numerical experiments in supersonic boundary layer stability. *Phys. Fluids* A **2**, 94–104.

Goldstein, M. E. 1983 The evolution of Tollmien–Schlichting waves near a leading edge. *J. Fluid Mech.* **127**, 59–81.

Graziosi, P. 1999 An experimental investigation on stability and transition at Mach 3. PhD Dissertation, Department of Mechanical and Aerospace Engineering of Princeton University.

Hinze, J. O. 1975 *Turbulence*, 2nd edn. McGraw-Hill.

Kachanov, Y. S. 1994 Physical mechanisms of laminar-boundary-layer transition. *Annu. Rev. Fluid Mech.* **26**, 411–482.

Kendall, J. M. 1967 Supersonic boundary layer stability experiments. *Boundary Layer Transition Study Group Meeting*, *Rep.* BSD-TR-67-213, vol. II, pp. 10-1–10-8.

Kendall, J. M. 1975 Wind tunnel experiments relating to supersonic and hypersonic boundary layer transition. *AIAA J.* **13**, 290–299.

KIMMEL, R. L. & KENDALL, J. M. 1990 Nonlinear disturbances in a hypersonic laminar boundary layer. *AIAA Paper* 90-0320.

KOSINOV, A. D., SEMIONOV, N. V., SHEVELKOV, S. G. & ZININ, O. I. 1994 Experiments of the nonlinear instability of supersonic boundary layers. In *Nonlinear Instability of Nonparallel Flows* (eds S. P. Lin, W. R. C. Phillips & D. T. Valentine), pp. 196–205. Springer.

KOVASZNAY, L. S. G. 1953 Turbulence in supersonic flow. *J. Aero. Sci.* **20**, 657–674 (682).

LAM, S. H. & ROTT, N. 1960 Theory of linearized time-dependent boundary layers. *Rep. AFOSR TN*-60-1100. Cornell Univ., Grad. School of Aero. Engng.

LAUFER, J. 1954 Factors affecting transition Reynolds numbers on models in supersonic wind tunnels. *J. Aero. Sci.* **21**, 497–498.

LAUFER, J. 1961 Aerodynamic noise in supersonic wind tunnels. *J. Aero. Sci.* **28**, 685–692.

LAUFER, J. 1964 Some statistical properties of the radiated pressure field generated by a supersonic turbulent boundary layer. *Phys. Fluids* **7**, 1191–1197.

LAUFER, J. & VREBALOVICH, T. 1960 Stability and transition of a supersonic laminar boundary layer on an insulated flat plate. *J. Fluid Mech.* **9**, 257–299.

LEBIGA, V. A., MASLOV, A. A. & PRIDANOV, V. G. 1979 Experimental investigation of the stability of supersonic boundary layer on a flat insulated plate. *Arch. Mech.* **31**, 397–405.

LEES, L. 1947 The stability of the laminar boundary layer in a compressible fluid. *NACA Tech. Note*, 1360.

LIN, R.-S., EDWARDS, J. R., WANG, W.-P. & MALIK, M. R. 1996 Instabilities of a Mach 2.4 slow-expansion square nozzle flow. *AIAA Paper* 96-0784.

MACK, L. M. 1975 Linear stability theory and the problem of supersonic boundary-layer transition. *AIAA J.* **3**, 278–289.

MACK, L. M. 1984 Boundary-layer linear stability theory. *Special Course on Stability and Transition of Laminar Flow. AGARD Rep.* 709, 1–81.

MASAD, J. A. & NAYFEH, A. H. 1990 Subharmonic instability of compressible boundary layers. *Phys. Fluids* A **2**, 1380–1392.

MORKOVIN, M. V. 1957 On transition experiments at moderate supersonic speeds. *J. Aero. Sci.* **24**, 480–486.

MORKOVIN, M. V. 1959 On supersonic wind tunnels with low free-stream disturbances. *Trans. ASME*: *J. Appl. Mech.* **26**, 319–324.

NG, L. & ERLEBACHER, G. 1992 Secondary instabilities in compressible boundary layers. *Phys. Fluids* A **4**, 710–726.

PATE, S. R. & SCHUELER, C. J. 1969 Radiated aerodynamic noise effects on boundary layer transition in supersonic and hypersonic wind tunnels. *AIAA J.* **7**, 450–457.

PRESS, W. H., TEUKOLSKY, S. A., VETTERLING, W. T. & FLANNERY, B. P. 1992 *Numerical Recipes in FORTRAN: The Art of Scientific Computing*, 2nd edn. Cambridge University Press.

PRUETT, C. D. & CHANG, C.-L. 1993 A comparison of PSE and DNS for high-speed boundary layer flows. FED-Vol. 151, In *Transitional and Turbulent Compressible Flows*. pp. 57–67. ASME.

PRUETT, C. D. & ZANG, T. A. 1992 Direct numerical simulation of laminar breakdown in high-speed, axisymmetric boundary layers. *Theor. Comput. Fluid Dyn.* **3**, 345–367.

REED, H. L., KIMMEL, R., SCHNEIDER, S. P. & ARNAL, D. 1997 Drag prediction and transition in hypersonic flow. *AIAA Paper* 97-1818.

RESHOTKO, E. 1994 Boundary layer instability, transition and control. The 1994 Dryden lecture in research. *AIAA Paper* 94-0001.

SCHNEIDER, S. P. 2001 Hypersonic laminar instability on round cones near zero angle of attack. *AIAA Paper* 01-0206.

SMITS, A. J., HAYAKAWA, K. & MUCK, K. C. 1983 Constant temperature hot-wire anemometer practice in supersonic flows. *Exps. Fluids* **1**, 83–92.

THUMM, A., WOLZ, W. & FASEL, H. 1989 Numerical simulation of spatially growing three-dimensional disturbance waves in compressible boundary layers. *Proc. Third IUTAM Symp. on Laminar-Turbulent Transition, Toulouse, France* (ed. D. Arnal & R. Michel), pp. 303–308. Springer.

TUMIN, A. M. & FEDOROV, A. V. 1982 Weakly nonparallel effects on stability characteristics. *Uchenye Zapiski TsAGI* **13**, 91–96 (in Russian).